

Observing the Galaxy's massive black hole with gravitational wave bursts

C. P. L. Berry¹* and J. R. Gair¹

¹*Institute of Astronomy, University of Cambridge, Madingley Road, Cambridge, CB3 0HA*

19 July 2011

ABSTRACT

we present power law fits to sketch out the dependence of the uncertainty on SNR, albeit approximately.

Key words: black hole physics – Galaxy: centre – gravitational waves – methods: data analysis.

1 BACKGROUND AND INTRODUCTION

Many, if not all, galactic nuclei have harboured a massive black hole (MBH) during their evolution (Lynden-Bell & Rees 1971; Soltan 1982; Rees 1984). Observations have shown there exist well-defined correlations between the MBHs' masses and the properties of their host galaxies, such as bulge luminosity, mass, velocity dispersion and light concentration (Kormendy & Richstone 1995; Magorrian et al. 1998; Ferrarese & Merritt 2000; Gebhardt et al. 2000; Graham et al. 2001; Tremaine et al. 2002; Marconi & Hunt 2003; Häring & Rix 2004; Graham 2007; Graham et al. 2011). These suggest coeval evolution of the MBH and galaxy, possibly with feedback mechanisms coupling the two (Haiman & Quataert 2004; Volonteri & Natarajan 2009). The MBH and the surrounding spheroidal galaxy share a common history, such that the growth of one can inform us about the growth of the other.

The best opportunity to study MBHs comes from the compact object in our own galactic centre (GC), which is coincident with Sagittarius A* (Sgr A*). This is identified as an MBH of mass $M_\bullet = 4.31 \times 10^6 M_\odot$ at a distance of only $R_0 = 8.33$ kpc (Gillessen et al. 2009).

According to the no-hair theorem, the MBH should be described completely by just its mass M_\bullet and spin a , since we expect the charge of an astrophysical black hole to be negligible (Israel 1967, 1968; Carter 1971; Hawking 1972; Robinson 1975; Chandrasekhar 1998). The spin parameter a is related to the BH's angular momentum J by

$$J = M_\bullet a c; \quad (1)$$

it is often convenient to use the dimensionless spin

$$a_* = \frac{cJ}{GM_\bullet^2}. \quad (2)$$

* E-mail: cplb2@cam.ac.uk

As we have a good estimate of the mass, to gain a full description of the MBH we have only to measure its spin; this will give us insight into its history and role in the evolution of the Galaxy.

The spin of an MBH is determined by several competing processes. An MBH accumulates mass and angular momentum through accretion (Volonteri 2010). Accretion from a gaseous disc will spin up the MBH, potentially leading to high spin values (Volonteri et al. 2005), while a series of randomly orientated accretion events will lead to a low spin value: we expect an average value $|a_*| \sim 0.1\text{--}0.3$ (King & Pringle 2006; King, Pringle & Hofmann 2008). The MBH will also grow through mergers (Yu & Tremaine 2002; Malbon et al. 2007). Minor mergers with smaller black holes (BHs) can decrease the spin (Hughes & Blandford 2003; Gammie, Shapiro & McKinney 2004), while a series of major mergers, between similar mass MBHs, would lead to a likely spin of $|a_*| \sim 0.69$ (Berti & Volonteri 2008; Berti et al. 2007; González et al. 2007). Measuring the spin of MBHs will help us understand the relative importance of these processes, and perhaps gain a glimpse into their host galaxies' pasts.

Elliptical and spiral galaxies are expected to host MBHs of differing spins because of their different evolutions: we expect MBHs in elliptical galaxies to have on average higher spins than black holes in spiral galaxies, where random, small accretion episodes have played a more important role (Volonteri, Sikora & Lasota 2007; Sikora, Stawarz & Lasota 2007).

It has been suggested that the spin of the Galaxy's MBH could be inferred from careful observation of the orbits of stars within a few milliparsecs of the GC (Merritt et al. 2010), although this is complicated because of perturbations due to other stars, or from observations of quasi-periodic oscillations (QPOs) in the luminosity of flares believed to originate from material orbiting close to the innermost stable orbits (Genzel et al. 2003; Bélanger et al. 2006; Trippe et al.

2007; Hamaus et al. 2009; Kato et al. 2010), though there are difficulties in interpreting these results (Psaltis 2008).

This latter method, combined with a disc-seismology model, has produced a value of the dimensionless spin of $a_* = 0.44 \pm 0.08$. To obtain this result Kato et al. (2010) have combined their observations of Sgr A* with observations of galactic X-ray sources containing solar mass BHs, to find a best-fit unique spin parameter for all BHs. However, it is not clear that all BHs should share the same value of the spin parameter; especially considering that the BHs considered here differ in mass by six orders of magnitude, with none in the intermediate range. Even if BH spin is determined by a universal process, we still expect some distribution of spin parameters (King et al. 2008; Berti & Volonteri 2008). Thus we cannot precisely determine the spin of the galactic centre’s MBH from an average including other BHs.

The spins of MBHs in active galactic nuclei have been inferred using X-ray observations of Fe K emission lines (Miller 2007; McClintock et al. 2011). So far this has been done for a handful of other galaxies’ central MBHs (Brenneman & Reynolds 2006; Miniutti et al. 2009; Schmoll et al. 2009; de la Calle Pérez et al. 2010; Zoghbi et al. 2010; Nardini et al. 2011; Patrick et al. 2011). Estimates for the spin cover a range of values up to the maximal value for an extremal Kerr black hole. Typical values are in the intermediate range of $a_* \sim 0.7$ with an uncertainty of about 10% on each measurement.

While we can use the spin of other BHs as a prior, to inform us of what we should expect to measure for the spin of the Galaxy’s MBH, it is desirable to have an independent observation, a direct measurement.

An exciting means of inferring information about the MBH is through gravitational waves (GWs) emitted when compact objects (COs), such as stellar mass BHs, neutron stars (NSs), white dwarfs (WDs) or low mass main sequence (MS) stars, pass close by (Sathyaprakash & Schutz 2009). The proposed Laser Interferometer Space Antenna (LISA) mission is designed to be able to detect GWs in the frequency range of interest for these encounters (Bender et al. 1998; Danzmann & Rüdiger 2003). The identification of waves requires a set of accurate waveform templates covering parameter space. Much work has already been done on the waveforms generated when companion objects inspiral towards an MBH (Glampedakis 2005); as they orbit, the GWs carry away energy and angular momentum, causing the orbit to shrink until eventually the object plunges into the MBH. The initial orbits may be highly elliptical and a burst of radiation is emitted during each close encounter. These are known as extreme mass-ratio bursts (EMRBs; Rubbo et al. 2006). Assuming that the companion is not scattered from its orbit, and does not plunge straight into the MBH, its orbit will evolve, becoming more circular, and it will begin to continuously emit significant gravitational radiation in the LISA frequency range. The resulting signals are known as extreme mass-ratio inspirals (EMRIs; Amaro-Seoane et al. 2007).

Studies of these systems have usually focused upon when the orbit completes multiple cycles, allowing a high signal-to-noise ratio to be accumulated. Here, we will investigate what can be learnt from high eccentricity orbits. These are the initial bursting orbits from which an EMRI may evolve. The event rate for the detection of

such EMRBs with LISA has been estimated to be as high as 15 yr^{-1} (Rubbo, Holley-Bockelmann & Finn 2006), although this has been revised downwards to the order of 1 yr^{-1} (Hopman, Freitag & Larson 2007). Even if only a single burst is detected during the LISA mission, this is still an exciting possibility since the information carried by the GW should give an unparalleled probe of the structure of spacetime of the GC. Exactly what can be inferred will depend upon the orbit.

We will make the simplifying assumption that all these orbits are marginally bound, or parabolic, since highly eccentric orbits will appear almost indistinguishable from an appropriate parabolic orbit. Here “parabolic” and “eccentricity” refer to the energy of the geodesic and not to the geometric shape of the orbit.¹ Following such a trajectory an object may make just one pass of the MBH or, if the periapsis distance is small enough, it may complete a number of rotations. Such an orbit is referred to as zoom-whirl (Glampedakis & Kennefick 2002).

In order to compute the gravitational waveform produced in such a case, we integrate the geodesic equations for a parabolic orbit in Kerr spacetime. We assume that the orbiting body is a test particle, such that it does not influence the underlying spacetime, and that the orbital parameters evolve negligibly during the orbit so that they may be held constant. We use this to construct an approximate numerical kludge waveform (Babak et al. 2007).

This paper is organised as follows. In Sec. 2 we discuss the construction of the geodesic orbits, in Sec. 3 we explain how to construct a numerical kludge waveform from this trajectory. In Sec. 4 we establish what the LISA detectors would measure, and in Sec. 5 and Sec. 6 how the signal would be analysed to extract the information encoded, and how this can be used to infer parameters. Results obtained using our waveform model to estimate the accuracy to which parameters could be measured are presented in Sec. 7. We give fiducial power-law fits for signal-to-noise ratio (SNR) as a function of periapse radius, and parameter uncertainty as a function of SNR, which may be of use for back-of-the-envelope estimates. We confirm the accuracy of the kludge waveforms in Sec. 8 by comparing the energy flux to fluxes calculated using other approaches. We conclude in Sec. 9 with a summary of our results. An appendix is included on the use of window functions to reduce spectral leakage when analysing waveforms. In this we present a novel window function, the Planck-Bessel window, which may be of use for signals with a large dynamic range.

Throughout this work we will assume metric with signature $(+,-,-,-)$. Greek indices are used to represent spacetime indices $\mu = \{0, 1, 2, 3\}$ and lowercase Latin indices from the middle of the alphabet are used for spatial indices $i = \{1, 2, 3\}$. Uppercase Latin indices from the beginning of the alphabet will be used for the output of two LISA detector-arms $A = \{\text{I}, \text{II}\}$, and lowercase Latin indices from the beginning of the alphabet are used for parameter space. Summation over repeated indices is assumed unless explicitly noted otherwise. Geometric units with $G = c = 1$ will

¹ Marginally bound Keplerian orbits in flat spacetime are parabolic in both senses.

be used where noted, but in general factors of G and c will be retained.

2 PARABOLIC ORBITS IN KERR SPACETIME

2.1 The metric and geodesic equations

Astrophysical BHs are described by the Kerr metric (Kerr 1963). In standard Boyer-Lindquist coordinates the line element is (Boyer & Lindquist 1967; Hobson, Efstathiou & Lasenby 2006, section 13.7)

$$ds^2 = \frac{\rho^2 \Delta}{\Sigma^2} c^2 dt^2 - \frac{\Sigma \sin^2 \theta}{\rho^2} (d\phi - \omega dt)^2 - \frac{\rho^2}{\Delta} dr^2 - \rho^2 d\theta^2, \quad (3)$$

where we have introduced functions

$$\rho^2 = r^2 + a^2 \cos^2 \theta, \quad (4)$$

$$\Delta = r^2 - \frac{2GM_\bullet r}{c^2} + a^2, \quad (5)$$

$$\Sigma = (r^2 + a^2)^2 - a^2 \Delta \sin^2 \theta, \quad (6)$$

$$\omega = \frac{2GM_\bullet ar}{c\Sigma}. \quad (7)$$

For the remainder of this section we shall work in natural units with $G = c = 1$.

Geodesics are parametrized by three conserved quantities (aside from the particle's mass μ): energy (per unit mass) E , specific angular momentum about the symmetry axis (the z -axis) L_z , and Carter constant Q (Carter 1968; Chandrasekhar 1998, section 62). The geodesic equations are

$$\rho^2 \frac{dt}{d\tau} = a(L_z - aE \sin^2 \theta) + \frac{r^2 + a^2}{\Delta} T, \quad (8)$$

$$\rho^2 \frac{dr}{d\tau} = \pm \sqrt{V_r}, \quad (9)$$

$$\rho^2 \frac{d\theta}{d\tau} = \pm \sqrt{V_\theta}, \quad (10)$$

$$\rho^2 \frac{d\phi}{d\tau} = \frac{L_z}{\sin^2 \theta} - aE + \frac{a}{\Delta} T, \quad (11)$$

where we have introduced potentials

$$T = E(r^2 + a^2) - aL_z, \quad (12)$$

$$V_r = T^2 - \Delta[r^2 + (L_z - aE)^2 + Q], \quad (13)$$

$$V_\theta = Q - \cos^2 \theta \left[a^2(1 - E^2) + \frac{L_z^2}{\sin^2 \theta} \right], \quad (14)$$

and τ is proper time. The signs of the r and θ equations may be chosen independently.

For a parabolic orbit $E = 1$; the particle is at rest at infinity. This simplifies the geodesic equations. It also allows us to give a simple interpretation for the Carter constant: this is defined as

$$Q = L_\theta^2 + \cos^2 \theta \left[a^2(1 - E^2) + \frac{L_z^2}{\sin^2 \theta} \right], \quad (15)$$

where L_θ is the (non-conserved) specific angular momentum in the θ -direction ($V_\theta = L_\theta^2$). For $E = 1$ we have

$$Q = L_\theta^2 + \cot^2 \theta L_z^2 = L_\infty^2 - L_z^2, \quad (16)$$

here L_∞ is the total specific angular momentum at infinity,

where the metric is asymptotically flat (de Felice 1980).² This is as in Schwarzschild spacetime.

2.2 Integration variables and turning points

In integrating the geodesic equations, difficulties can arise because of the presence of turning points in the motion, when the sign of the r or θ geodesic equation will change. The radial turning points are at the periapsis r_p and at infinity. We may locate the periapsis by finding the roots of

$$V_r = 2M_\bullet r^3 - (L_z^2 + Q)r^2 + 2M_\bullet [(L_z - a)^2 + Q]r - a^2 Q = 0. \quad (17)$$

This has three roots, which we shall denote $\{r_1, r_2, r_p\}$; the periapsis r_p is the largest real root. We do not find the apoapsis as a (fourth) root to this equation as we have removed it by taking $E = 1$ before solving. This turning point can be found by setting the unconstrained expression for V_r equal to zero, and then solving for $E(r)$; taking the limit $r \rightarrow \infty$ gives $E \rightarrow 1$ (Wilkins 1972).

We may avoid the difficulties associated with the turning point by introducing an angular variable that always increases with proper time (Drasco & Hughes 2004): inspired by Keplerian orbits, we parametrize our trajectory by

$$r = \frac{p}{1 + e \cos \psi}, \quad (18)$$

where $e = 1$ is the eccentricity and $p = 2r_p$ is the semilatus rectum. As ψ covers its full range from $-\pi$ to π , r traces out one full orbit from infinity through the periapsis at $\psi = 0$ back to infinity. The geodesic equation for ψ is

$$\rho^2 \frac{d\psi}{d\tau} = \left\{ M_\bullet \left[2r_p - (r_1 + r_2)(1 + \cos \psi) + \frac{r_1 r_2}{2r_p} (1 + \cos \psi)^2 \right] \right\}^{1/2}. \quad (19)$$

This may be integrated without problem. Parametrizing an orbit by its periapsis and eccentricity has the additional benefit of allowing easier comparison with its flat-space equivalent (Gair, Kennefick & Larson 2005).

The θ motion is usually bounded, with $\theta_0 \leq \theta \leq \pi - \theta_0$; in the event that $L_z = 0$ the particle follows a polar orbit and θ will cover its full range. The turning points are given by

$$V_\theta = Q - \cot^2 \theta L_z^2 = 0. \quad (20)$$

Only if $L_z = 0$ may we reach the poles (Wilkins 1972). If we change variable to $\zeta = \cos^2 \theta$, we have a maximum value $\zeta_0 = \cos^2 \theta_0$ given by

$$\zeta_0 = \frac{Q}{Q + L_z^2} = \frac{Q}{L_\infty^2}. \quad (21)$$

See Fig. 1 for a geometrical visualization. Let us now introduce a second angular variable (Drasco & Hughes 2004)

$$\zeta = \zeta_0 \cos^2 \chi. \quad (22)$$

² See Rosquist, Bylund & Samuelsson (2009) for a discussion of the interpretation of Q in the limit $G \rightarrow 0$, corresponding to a flat spacetime.

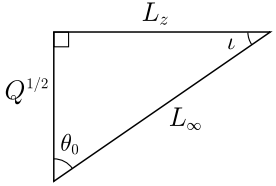


Figure 1. The angular momenta L_∞ , L_z and \sqrt{Q} define a right-angled triangle. The acute angles are θ_0 , the extremal value of the polar angle, and ι , the orbital inclination (Glampedakis, Hughes & Kennefick 2002).

Over one 2π period of χ , θ oscillates over its full range, from its minimum value to its maximum and back. The geodesic equation for χ is

$$\rho^2 \frac{d\chi}{d\tau} = \sqrt{Q + L_z^2}, \quad (23)$$

and may be integrated simply.

3 WAVEFORM CONSTRUCTION

For given angular momenta L_z and Q , and initial starting position, we can calculate the geodesic trajectory. The orbiting body is assumed to follow this track exactly; we ignore evolution due to the radiation of energy and angular momentum, which should be negligible for EMRBs. From this trajectory we calculate the waveform using a semirelativistic approximation (Ruffini & Sasaki 1981): we assume that the particle moves along a geodesic in the Kerr geometry, but radiates as if it were in flat spacetime. This quick-and-dirty technique is known as a numerical kludge (NK), and has been shown to approximate well results computed by more accurate methods (Babak et al. 2007).

3.1 Kludge approximation

Numerical kludge approximations aim to encapsulate the main characteristics of a waveform by using the exact particle trajectory (ignoring inaccuracies from radiative effects and from the particle's self-force), whilst saving on computational time by using approximate waveform generation techniques.

To start, we build an equivalent flat-space trajectory from the Kerr geodesic. This is done by identifying the Boyer-Lindquist coordinates with a set of flat-space coordinates. We consider two choices here:

- (i) Identify the Boyer-Lindquist coordinates with flat-space spherical polars $\{r_{\text{BL}}, \theta_{\text{BL}}, \phi_{\text{BL}}\} \rightarrow \{r_{\text{sph}}, \theta_{\text{sph}}, \phi_{\text{sph}}\}$, then define flat-space Cartesian coordinates (Gair et al. 2005; Babak et al. 2007)

$$\mathbf{x} = \begin{pmatrix} r_{\text{sph}} \sin \theta_{\text{sph}} \cos \phi_{\text{sph}} \\ r_{\text{sph}} \sin \theta_{\text{sph}} \sin \phi_{\text{sph}} \\ r_{\text{sph}} \cos \theta_{\text{sph}} \end{pmatrix}. \quad (24)$$

- (ii) Identify the Boyer-Lindquist coordinates with flat-space oblate-spheroidal coordinates $\{r_{\text{BL}}, \theta_{\text{BL}}, \phi_{\text{BL}}\} \rightarrow \{r_{\text{ob}}, \theta_{\text{ob}}, \phi_{\text{ob}}\}$ so that the flat-space Cartesian coordinates

are

$$\mathbf{x} = \begin{pmatrix} \sqrt{r_{\text{ob}}^2 + a^2} \sin \theta_{\text{ob}} \cos \phi_{\text{ob}} \\ \sqrt{r_{\text{ob}}^2 + a^2} \sin \theta_{\text{ob}} \sin \phi_{\text{ob}} \\ r_{\text{ob}} \cos \theta_{\text{ob}} \end{pmatrix}. \quad (25)$$

These are appealing because in the limit that $G \rightarrow 0$, where the gravitating mass goes to zero, the Kerr metric in Boyer-Lindquist coordinates reduces to the Minkowski metric in oblate-spheroidal coordinates.

In the limit of $a \rightarrow 0$, the two coincide, as they do in the limit of large r .

It must be stressed that there is no well motivated argument that either coordinate system must yield an accurate GW; their use is justified *post facto* by comparison with results obtained from more accurate, and computationally intensive, methods (Gair et al. 2005; Babak et al. 2007). The ambiguity in assigning flat-space coordinates reflects the inconsistency of the semirelativistic approximation: the geodesic trajectory was calculated for the Kerr geometry; by moving to flat spacetime we lose the reason for its existence. However, this inconsistency should not be regarded as a major problem; it is just an artifact of the basic assumption that the shape of the trajectory is important for determining the character of the radiation, but the curvature of the spacetime in the vicinity of the source is not. By binding the particle to the exact geodesic, we ensure that the kludge waveform has spectral components at the correct frequencies, but by assuming flat spacetime for generation of GWs they will not have the correct amplitudes.

3.2 Quadrupole-octupole formula

Now we have a flat-space particle trajectory $x_p^\mu(\tau)$, we may apply a flat-space wave generation formula. We shall use the quadrupole-octupole formula to calculate the gravitational strain (Bekenstein 1973; Press 1977; Yunes et al. 2008)

$$h^{jk}(t, \mathbf{x}) = -\frac{2G}{c^6 r} \left(\ddot{I}^{jk} - 2n_i \ddot{S}^{ijk} + n_i \dot{M}^{ijk} \right)_{t' = t - r/c}, \quad (26)$$

where an over-dot represents differentiation with respect to time t (and not τ), t' is the retarded time, $r = |\mathbf{x} - \mathbf{x}_p|$ is the radial distance, \mathbf{n} is the radial unit vector, and the mass quadrupole I^{jk} , current quadrupole S^{ijk} and mass octupole M^{ijk} are defined by

$$I^{jk}(t') = \int x'^j x'^k T^{00}(t', \mathbf{x}') d^3x'; \quad (27)$$

$$S^{ijk}(t') = \int x'^j x'^k T^{0i}(t', \mathbf{x}') d^3x'; \quad (28)$$

$$M^{ijk}(t') = \frac{1}{c} \int x'^i x'^j x'^k T^{00}(t', \mathbf{x}') d^3x'. \quad (29)$$

This is correct for a slowly moving source. It is the familiar quadrupole formula (Misner, Thorne & Wheeler 1973, section 36.10; Hobson et al. 2006, section 17.9), derived from linearized theory, plus the next order terms. For a point mass, the energy-momentum tensor $T^{\mu\nu}$ contains a δ -function which allows easy evaluation of the integrals of the various moments to give

$$I^{jk} = c^2 \mu x_p^j x_p^k; \quad (30)$$

$$S^{ijk} = c \mu v_p^i x_p^j x_p^k; \quad (31)$$

$$M^{ijk} = c \mu x_p^i x_p^j x_p^k. \quad (32)$$

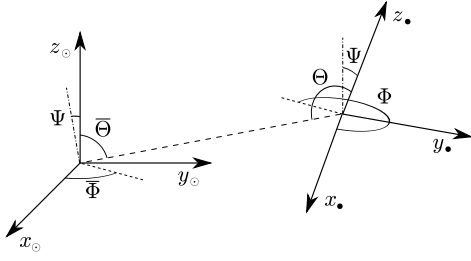


Figure 2. The relationship between the MBH's coordinate system x_\bullet^i and the SS coordinate system x_\odot^i . The MBH's spin axis is aligned with the z_\bullet -axis.

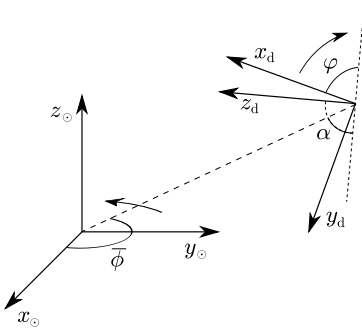


Figure 3. The relationship between the detector coordinates x_d^i and the ecliptic coordinates of the SS x_\odot^i (Bender et al. 1998).

Since we are only interested in GWs, we shall use the transverse-traceless (TT) gauge. The waveform is given in the TT gauge by (Misner et al. 1973, box 35.1)

$$h_{jk}^{\text{TT}} = P_j^l h_{lm} P_k^m - \frac{1}{2} P_{jk} P^{lm} h_{lm}, \quad (33)$$

where the (spatial) projection operator P_{ij} is

$$P_{ij} = \delta_{ij} - n_i n_j. \quad (34)$$

4 DETECTION WITH LISA

The classic LISA design is a three arm, space-borne laser interferometer (Bender et al. 1998; Danzmann & Rüdiger 2003). The three arms form an equilateral triangle that rotates as the system's centre of mass follows a circular, heliocentric orbit, trailing 20° behind the Earth. To describe the detector configuration, and to transform from the MBH coordinate system to those of the detector, we will find it useful to define three coordinate systems: those of the BH at the GC x_\bullet^i ; ecliptic coordinates centred at the solar system (SS) barycentre x_\odot^i , and coordinates that co-rotate with the detector x_d^i . The MBH's coordinate system and the SS coordinate system are depicted in Fig. 2. The currently envisioned LISA mission geometry is shown in Fig. 3. We define the detector coordinates such that the detector-arms lie in the x_d - y_d plane as shown in Fig. 4. The coordinate systems are related by a series of angles: Θ and Φ give the orientation of the SS in the MBH's coordinates. These define the orientation of the MBH's spin axis z_\bullet . $\bar{\Theta}$ and $\bar{\Phi}$ give the position of the GC in ecliptic coordinates. The angle Ψ specifies the relative inclinations of the z -axes of the SS and MBH: their

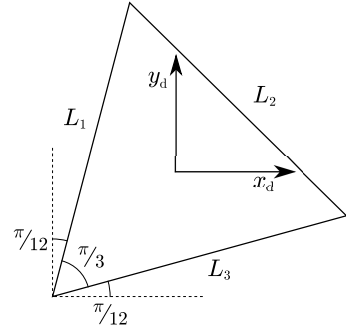


Figure 4. The alignment of the three detector arms, with lengths L_1 , L_2 and L_3 , within the x_d - y_d plane (Cutler 1998). The origin of the detector coordinates coincides with the centre of mass of the constellation of satellites.

orientation in the plane of the sky. $\bar{\phi}$ gives LISA's orbital phase and φ gives the rotational phase of the detector arms. Both of these vary linearly with time

$$\bar{\phi}(t) = \omega_\oplus t + \bar{\phi}_0; \quad \varphi(t) = -\omega_\oplus t + \varphi_0; \quad (35)$$

where ω_\oplus corresponds to one rotation per year. Finally, $\alpha = 60^\circ$ is the inclination of the detector plane. We have computed the waveforms in the MBH's coordinates, however it is simplest to describe the measured signal using the detector's coordinates.

The strains measured in the three arms can be combined such that LISA behaves as a pair of 90° interferometers at 45° to each other, with signals scaled by $\sqrt{3}/2$ (Cutler 1998). We will denote the two detectors as I and II. If we label the change in the three arms' lengths caused by GWs δL_1 , δL_2 and δL_3 , and use L for the unperturbed length, then detector I measures strain

$$h_{\text{I}}(t) = \frac{\delta L_1 - \delta L_2}{L} = \frac{\sqrt{3}}{2} \left(\frac{1}{2} h_{\text{d}}^{xx} - \frac{1}{2} h_{\text{d}}^{yy} \right), \quad (36)$$

and detector II measures

$$h_{\text{II}}(t) = \frac{\delta L_1 + \delta L_2 - 2\delta L_3}{\sqrt{3}L} = \frac{\sqrt{3}}{2} \left(\frac{1}{2} h_{\text{d}}^{xy} + \frac{1}{2} h_{\text{d}}^{yx} \right). \quad (37)$$

We will use vector notation $\mathbf{h}(t) = (h_{\text{I}}(t), h_{\text{II}}(t)) = \{h_A(t)\}$ to represent signals from both detectors.

The final consideration for calculating the signal measured by LISA is the time of arrival of the signal: LISA's orbital position changes with time. Fortunately over the timescales of interest for parabolic encounters, these changes are small. We will assume that the position of the SS barycentre relative to the GC is constant: it is defined by the distance R_0 and the angles $\bar{\Theta}$ and $\bar{\Phi}$. The time of arrival at the SS barycentre t_\odot is then the retarded time; the time of detection t_{d} to lowest order is

$$t_{\text{d}} \simeq t_\odot - t_{\text{AU}} \cos [\bar{\phi}(t_\odot) - \bar{\Phi}] \sin \bar{\Theta}, \quad (38)$$

where t_{AU} is the light travel-time for LISA's orbital radius. The time t_{d} is required for $\phi(t)$ and $\varphi(t)$.

5 SIGNAL ANALYSIS

5.1 Frequency domain formalism

Having constructed the GW $\mathbf{h}(t)$ that will be incident upon the LISA detector, we may now consider how to analyse the waveform and extract the information it contains. We begin with a brief overview of the basic components of signal analysis used for GWs, with application to LISA in particular. This fixes notation. A more complete discussion of the material can be found in the work of Finn (1992), and Cutler & Flanagan (1994).

The measured strain $\mathbf{s}(t)$ will be the combination of the signal and the detector noise

$$\mathbf{s}(t) = \mathbf{h}(t) + \mathbf{n}(t); \quad (39)$$

we will assume that the noise $n_A(t)$ is stationary and Gaussian. When analysing signals, it is most convenient to work with the Fourier transform

$$\tilde{g}(f) = \mathcal{F}\{g(t)\} = \int_{-\infty}^{\infty} g(t) e^{2\pi i f t} dt. \quad (40)$$

For a Gaussian noise signal $n_A(t)$, each Fourier component $\tilde{n}_A(f)$ also has a Gaussian probability distribution; the assumption of stationarity means that different Fourier components are uncorrelated, thus (Cutler & Flanagan 1994)

$$\langle \tilde{n}_A(f) \tilde{n}_B^*(f') \rangle_n = \frac{1}{2} \delta(f - f') S_{AB}(f), \quad (41)$$

where $\langle \dots \rangle_n$ denotes the expectation value over the noise distribution, and $S_{AB}(f)$ is the (single-sided) noise spectral density. For simplicity, we may assume that the noise in the two detectors is uncorrelated, but share the same characterisation so that (Cutler 1998)

$$S_{AB}(f) = S_n(f) \delta_{AB}. \quad (42)$$

The functional form of the noise spectral density $S_n(f)$ for LISA is discussed in Sec. 5.2.

The properties of the noise allow us to define a natural inner product and associated distance on the space of signals (Cutler & Flanagan 1994)

$$(\mathbf{g}|\mathbf{k}) = 2 \int_0^{\infty} \frac{\tilde{g}_A^*(f) \tilde{k}_A(f) + \tilde{g}_A(f) \tilde{k}_A^*(f)}{S_n(f)} df. \quad (43)$$

Using this definition, the signal-to-noise ratio is approximately

$$\rho[\mathbf{h}] = (\mathbf{h}|\mathbf{h})^{1/2}. \quad (44)$$

The probability of a particular realization of noise $\mathbf{n}(t) = \mathbf{n}_0(t)$ is

$$p(\mathbf{n}(t) = \mathbf{n}_0(t)) \propto \exp \left[-\frac{1}{2} (\mathbf{n}_0|\mathbf{n}_0) \right]. \quad (45)$$

If the incident waveform is given as $\mathbf{h}(t)$, the probability of measuring signal $\mathbf{s}(t)$ is

$$p(\mathbf{s}(t)|\mathbf{h}(t)) \propto \exp \left[-\frac{1}{2} (\mathbf{s} - \mathbf{h}|\mathbf{s} - \mathbf{h}) \right]. \quad (46)$$

5.2 LISA noise curve

LISA's noise has two sources: instrumental noise and confusion noise, primarily from white dwarf binaries. The latter

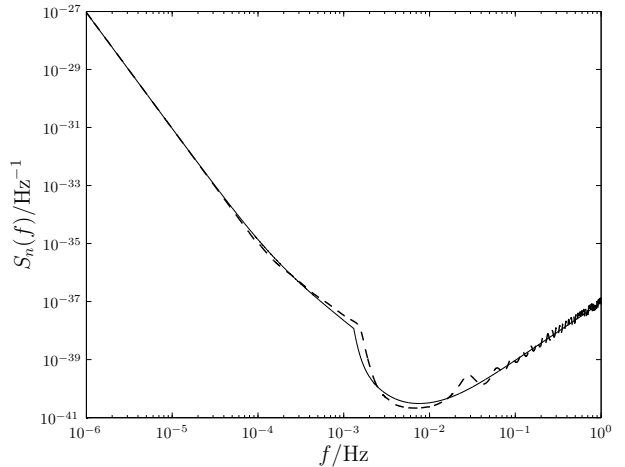


Figure 5. The LISA noise curve. The solid line indicates the analytic approximation of Barack & Cutler (2004) used in this work. For comparison, the dashed line is from the online sensitivity curve generator (<http://www.srl.caltech.edu/~shane/sensitivity/>; Larson, Hiscock & Hellings 2000; Larson, Hellings & Hiscock 2002). For parabolic encounters we are most interested in the low-frequency region where the two curves are the same.

may be divided into contributions from galactic and extra-galactic binaries. In this work we use the noise model of Barack & Cutler (2004). The shape of the noise curve can be seen in Fig. 5. The instrumental noise dominates at both high and low frequencies. The confusion noise is important at intermediate frequencies, and is responsible for the cusp around $f = 10^{-3}$ Hz.

5.3 Window functions

There is one remaining complication regarding signal analysis: since we are Fourier transforming a finite signal we encounter spectral leakage; a contribution from large amplitude spectral components leaks into surrounding components (sidelobes), obscuring and distorting the spectrum at these frequencies (Harris 1978). This is an inherent problem with finite signals; it will be as much of a problem when analysing signals from LISA as it is computing waveforms here. To mitigate, but unfortunately not eliminate, these effects, the time-domain signal can be multiplied by a window function. These are discussed in detail in Appendix A. We have adopted the Nuttall four-term window with continuous first derivative (Nuttall 1981) for the results presented here.

6 PARAMETER ESTIMATION AND WAVEFORMS

6.1 Model parameters

The shape of the waveform depends on a number of parameters: those defining the MBH; those defining the companion object on its orbit, and those defining the LISA detector. Let us define $\boldsymbol{\lambda} = \{\lambda^1, \lambda^2, \dots, \lambda^N\}$ as the set of N parameters which specify the GW. For our model, the input parameters are:

(1) The MBH's mass M_\bullet . This is currently well constrained by the observation of stellar orbits about Sgr A* (Ghez et al. 2008; Gillessen et al. 2009), with the best estimate being $M_\bullet = (4.31 \pm 0.36) \times 10^6 M_\odot$. However this depends upon the galactic centre distance R_0 being accurately known. If the uncertainty in this is included $M_\bullet = (3.95 \pm 0.06|_{\text{stat}} \pm 0.18|_{R_0, \text{stat}} \pm 0.31|_{R_0, \text{sys}}) \times 10^6 M_\odot (R_0/8 \text{ kpc})^{2.19}$, where the errors are statistical, independent of R_0 ; statistical from the determination of R_0 , and systematic from R_0 respectively.

(2) The spin parameter a_* . Naively this could be anywhere in the range $|a_*| < 1$; however it is possible to place an upper bound by contemplating spin-up mechanisms. Considering the torque from radiation emitted by an accretion disc, and swallowed by the BH, it can be shown that $|a_*| \lesssim 0.998$ (Thorne 1974). Magnetohydrodynamical simulations of accretion discs produce a smaller maximum value of $|a_*| \sim 0.95$ (Gammie et al. 2004). The actual spin value could be much lower than this upper bound depending upon the MBH's evolution (as discussed in Sec. 1). We will use the convention that a_* is positive, and will change the sense of rotation by flipping the z -axis.

(3) The polar angle Θ defining the propagation direction.

(4) The orientation angle Ψ . Since a_* is positive, this is in the range $[-\pi, \pi]$.

(5) The SS-GC distance R_0 . As for M_\bullet , this is constrained by stellar orbits, the best estimate being (Gillessen et al. 2009) $R_0 = 8.33 \pm 0.35$ kpc. We use the logarithm of R_0 in place of R_0 .

(6, 7) The coordinates of the MBH from the SS barycentre $\bar{\Theta}$ and $\bar{\Phi}$. These may be taken as the coordinates of Sgr A*, as the radio source is expected to be within ten Schwarzschild radii of the MBH (Reid et al. 2003; Doeleman et al. 2008). At the epoch J2000.0 $\bar{\Theta} = 95.607669^\circ$, $\bar{\Phi} = 266.851760^\circ$ (Reid et al. 1999). This will change with time due to the rotation of the SS about the GC, the proper motion is about 6 mas yr $^{-1}$, mostly in the plane of the galaxy (Reid et al. 1999; Backer & Sramek 1999; Reid et al. 2003).

(8) The angular momentum of the orbit about the MBH's spin axis L_z .

(9) The Carter constant for the orbit Q .

(10) The mass of the orbiting particle μ . This will depend upon the type of object: whether it is a MS star, WD, NS or BH.

(11–13) The initial position of the particle (x_0, y_0, z_0) . For specific values of Q and L_z there is a definite upper limit on $|z_0|/\sqrt{x_0^2 + y_0^2}$ given by the size of θ_0 from (21).

(14, 15) The orbital position of the LISA satellites given by $\bar{\phi}$ and φ . We will assume that the initial positions are chosen such that $\bar{\phi} = 0$ when $\varphi = 0$ (Cutler 1998), however this choice does not qualitatively influence our results.

The azimuthal angle Φ is omitted, since it arbitrarily defines the orientation of the MBH's x - and y -axes. We shall define it to be zero without loss of generality. We have a 15-dimensional parameter space. However, for a given signal arrival time the orbital parameters of LISA will be known; we will not try to infer these.

6.2 Waveforms

Figure 6.2 show example waveforms to demonstrate some of the possible variations in the signal. All these assume the standard mass and position for the MBH as well as a $\mu = 10M_\odot$ orbiting CO; other parameters are specified in the captions.

The plotted waveforms use the oblate-spheroidal coordinate system for the NK. Using spherical polars makes a small difference: on the scale shown here the only discernible difference would be in Fig. 6(a); in the other cases the difference is entirely negligible except in the high-frequency tail. The fractional difference for the orbit of Fig. 6(a) is shown in Fig. 6.2.

We conclude that the choice of coordinates for the kludge approximation is unimportant, and shall continue using oblate-spheroidal coordinates for the rest of this work.

6.3 Inference and Fisher matrices

Having detected a GW signal $\mathbf{s}(t)$, we are interested in what we can learn about the source. We have an inference problem that can be solved by appropriate application of Bayes' Theorem (Jaynes 2003, chapter 4): the probability distribution for our parameters given that we have detected the signal $\mathbf{s}(t)$ is given by the posterior

$$p(\boldsymbol{\lambda}|\mathbf{s}(t)) = \frac{p(\mathbf{s}(t)|\boldsymbol{\lambda})p(\boldsymbol{\lambda})}{p(\mathbf{s}(t))}. \quad (47)$$

Here $p(\mathbf{s}(t)|\boldsymbol{\lambda})$ is the likelihood of the parameters, $p(\boldsymbol{\lambda})$ is the prior probability distribution for the parameters, and $p(\mathbf{s}(t)) = \int p(\mathbf{s}(t)|\boldsymbol{\lambda}) d^N \boldsymbol{\lambda}$ is, for our purposes, a normalising constant and may be ignored. The likelihood function depends upon the realization of noise. A particular set of parameters $\boldsymbol{\lambda}_0$ defines a waveform $\mathbf{h}_0(t) = \mathbf{h}(t; \boldsymbol{\lambda}_0)$, the probability that we observe signal $\mathbf{s}(t)$ for this GW is given by (46), so the likelihood is

$$p(\mathbf{s}(t)|\boldsymbol{\lambda}_0) \propto \exp \left[-\frac{1}{2} (\mathbf{s} - \mathbf{h}_0 | \mathbf{s} - \mathbf{h}_0) \right]. \quad (48)$$

If we were to define this as a probability distribution for the parameters $\boldsymbol{\lambda}$, then the modal values would be the maximum-likelihood parameters $\boldsymbol{\lambda}_{\text{ML}}$. The waveform $\mathbf{h}(t; \boldsymbol{\lambda}_{\text{ML}})$ would be the signal closest to $\mathbf{s}(t)$ in the space of all signals, where distance is defined using the inner product (43) (Cutler & Flanagan 1994).

In the limit of a high SNR, we may approximate this as (Vallisneri 2008)

$$p(\mathbf{s}(t)|\boldsymbol{\lambda}_0) \propto \exp \left[-\frac{1}{2} (\partial_a \mathbf{h} | \partial_b \mathbf{h}) (\lambda^a - \langle \lambda^a \rangle_\ell) (\lambda^b - \langle \lambda^b \rangle_\ell) \right], \quad (49)$$

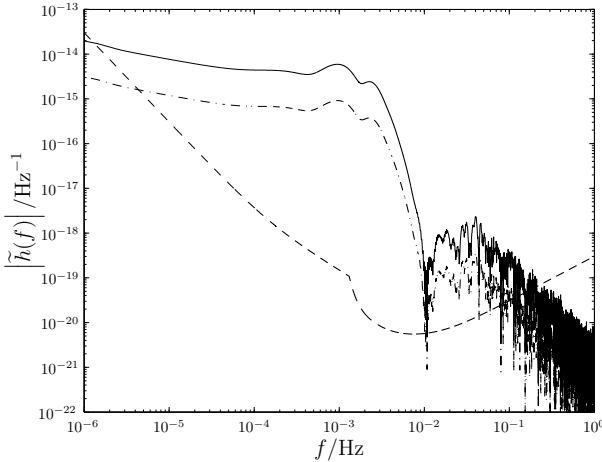
where the mean is defined as

$$\langle \lambda^a \rangle_\ell = \frac{\int \lambda^a p(\mathbf{s}(t)|\boldsymbol{\lambda}) d^N \boldsymbol{\lambda}}{\int p(\mathbf{s}(t)|\boldsymbol{\lambda}) d^N \boldsymbol{\lambda}}. \quad (50)$$

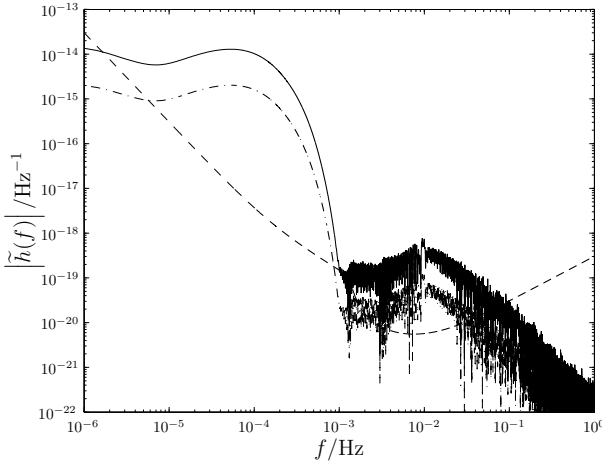
Using the high SNR limit, this is the maximum-likelihood value $\langle \lambda^a \rangle_\ell = \lambda_{\text{ML}}^a$. The quantity

$$\Gamma_{ab} = (\partial_a \mathbf{h} | \partial_b \mathbf{h}) \quad (51)$$

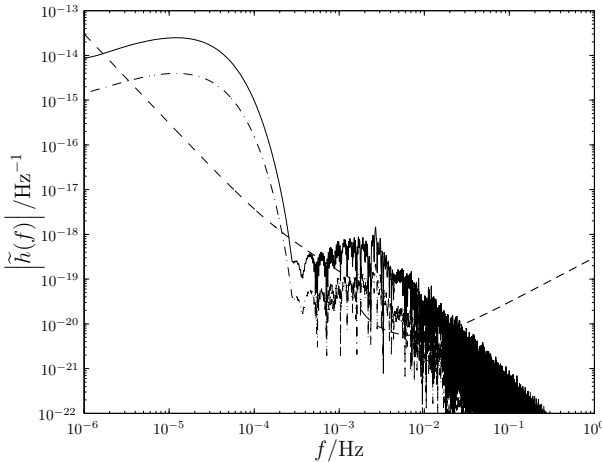
is the Fisher information matrix. It controls the variance of the likelihood distribution.



(a) Waveform for $a_* = 0.9$, $r_p = 1.75r_S$ and $\iota = 0.05$, with $\Theta = \pi/2$, $\Psi = \pi/4$. The SNR for the oblate-spheroidal kludge waveform (plotted) is $\rho[\mathbf{h}_{\text{ob}}] = 15600$, for the spherical polar kludge it is $\rho[\mathbf{h}_{\text{sph}}] = 14100$.



(b) Waveform for $a_* = 0.5$, $r_p = 10r_S$ and $\iota = 1.5$, with $\Theta = 0$ and $\Psi = 0$. The SNRs are $\rho[\mathbf{h}_{\text{sph}}] = 97.3$ and $\rho[\mathbf{h}_{\text{ob}}] = 97.1$.



(c) Waveform for $a_* = 0.3$, $r_p = 25r_S$ and $\iota = 0$, with $\Theta = \pi/3$ and $\Psi = \pi/6$. The SNRs are $\rho[\mathbf{h}_{\text{ob}}] = 10.7$ and $\rho[\mathbf{h}_{\text{sph}}] = 10.7$ (agreement to 0.01%).

Figure 6. Example burst waveforms from the galactic centre. The strain $\tilde{h}_1(f)$ is indicated by the solid line, $\tilde{h}_{\text{II}}(f)$ by the dot-dashed line, and the noise curve by the dashed line. The kludge has been formulated using oblate-spheroidal coordinates.

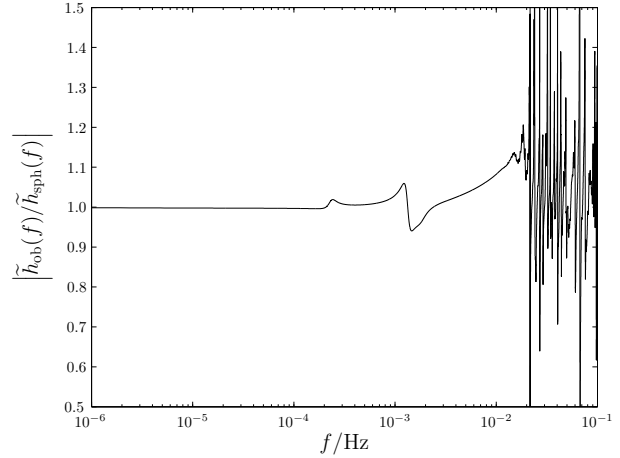


Figure 7. Comparison of waveforms generated using oblate-spheroidal and spherical polar coordinates for the numerical kludge. Both $\tilde{h}_1(f)$ and $\tilde{h}_{\text{II}}(f)$ show the same behaviour. The effects of spectral leakage are seen at high-frequencies.

The form of the posterior distribution will depend upon the nature of the prior information. If we have an uninformative prior, such that $p(\boldsymbol{\lambda})$ is a constant, then the posterior distribution would be determined by the likelihood. In the high SNR limit, we would obtain a Gaussian with variance-covariance matrix

$$\boldsymbol{\Sigma} = \boldsymbol{\Gamma}^{-1}. \quad (52)$$

The Fisher information matrix gives the uncertainty associated with the estimated parameter values, in this case the maximum-likelihood values.

If the prior were to restrict the allowed range for a parameter, for example, as is the case for the spin a_* , then the posterior would be a truncated Gaussian, and $\boldsymbol{\Gamma}^{-1}$ may no longer represent the variance-covariance.

If the prior were approximately Gaussian with variance-covariance matrix $\boldsymbol{\Sigma}_0$, then the posterior would also be Gaussian.³ The posterior variance-covariance would be (Cutler & Flanagan 1994; Vallisneri 2008)

$$\boldsymbol{\Sigma} = (\boldsymbol{\Gamma} + \boldsymbol{\Sigma}_0^{-1})^{-1}. \quad (53)$$

From this the inverse Fisher matrix $\boldsymbol{\Gamma}^{-1}$ is an upper bound on the size of the posterior covariance matrix.⁴

To understand what we can learn from parabolic encounters alone, we will look at the inverse Fisher matrix elements. If these are small then we expect we would be able to precisely determine a parameter, whereas if they are large we would not be able to learn much more than we already know from our prior.

³ If we only know the typical value and spread of a parameter then a Gaussian is the maximum entropy prior (Jaynes 2003, section 7.11): the prior that is least informative given what we do know.

⁴ It may also be shown to be the Cramér-Rao bound on the error covariance of an unbiased estimator (Cutler & Flanagan 1994; Vallisneri 2008). Thus it represents the frequentist error: the lower bound on the covariance for an unbiased parameter estimator $\boldsymbol{\lambda}_{\text{est}}$ calculated from an infinite set of experiments with the same signal $\mathbf{h}(t)$ but different realisations of the noise $\mathbf{n}(t)$.

7 RESULTS

7.1 Data set

To investigate the variation of inverse Fisher matrix elements for different orbits, waveforms were computed for a range of different orbits. In each case the massive black hole was assumed to have a mass of $M_\bullet = 4.31 \times 10^6 M_\odot$, and to be at the J2000.0 coordinates at a distance of $R_0 = 8.33$ kpc.

Four different spin values were chosen $a_* = 0, 0.3, 0.6, 0.9$. Waveforms were calculated for two different compact objects, one of mass $1.4M_\odot$ as appropriate for a neutron star, one of mass $10M_\odot$ represented a black hole. For each spin and mass, orbits with three different inclinations $\iota = \pi/12, \pi/4, 5\pi/12$ were calculated, each for both prograde and retrograde rotation.

Waveforms were computed for orbits with periapses uniformly separated in logarithmic space between $4r_S$ and $50r_S$, where $r_S = 2GM_\bullet/c^2$ corresponds to the Schwarzschild radius. For an initial run, six different radii were chosen. For a subsequent run, 20 different radii were randomly chosen for each spin, mass, inclination and sense of rotation.

In addition to this, the initial position, orientation of the MBH, and orbital position of LISA were varied: for each combination of MBH spin, compact object mass, inclination, rotation sense and periapsis, 20 random combinations of these intrinsic parameters (each being drawn from a separate uniform distribution over the permitted range) were used for the initial run, and 10 were used for the second run. The initial position was chosen such that the initial distance from the MBH was 10^{13} m $\simeq 785r_S$

7.2 Inverse Fisher matrices and SNR

From (26) we see that the amplitude of the waveform is proportional to the compact object mass μ . Consequently we expect there to be a proportionality between the SNR and the mass, from (44), $\rho[\mathbf{h}] \propto \mu$, and there to be an inverse proportionality between the elements of the variance-covariance matrix and the mass, from (51) and (52), $\Sigma_{ab} \propto \mu^{-2}$. We shall consider mass-scale values to give results independent of the compact object's mass. This will allow an easier combination of results from the computations for a NS and for a BH. From the variance-covariance matrix we can define the uncertainty for a particular parameter

$$\sigma_a = \sqrt{\Sigma_{aa}} \quad (\text{no summation}). \quad (54)$$

This should be proportional to μ^{-1} . We will denote the mass-normalised quantities

$$\hat{\rho}[\mathbf{h}] = \frac{\rho[\mathbf{h}]}{\mu}; \quad \hat{\sigma}_a = \mu\sigma_a. \quad (55)$$

We take the mean of $\ln \sigma_a$ and $\ln \rho$ for each set of randomised intrinsic parameters (starting position, MBH orientation and LISA orientation).⁵

There exists a correlation between the periapse radius and SNR, as shown in Fig. 8. Closer orbits produce louder

⁵ The logarithm is a better quantity to work with since both are positive-definite quantities that may be distributed over a range of magnitudes (MacKay 2003, sections 22.1, 23.3). Using median values yields results that are quantitatively similar.

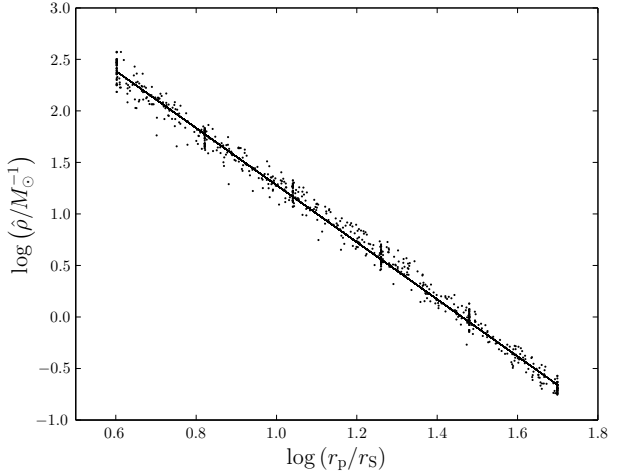


Figure 8. Mass-normalised SNR as a function of periapse radius. The plotted points are the values obtained by averaging over each set of intrinsic parameters. The best fit line is $\log(\hat{\rho}/M_\odot^{-1}) = -2.77 \log(r_p/r_S) + 4.05$. This has a reduced chi-squared value of $\chi^2/\nu = 1.64$.

bursts. To reflect this relationship, we have fitted a simple fiducial power law, as indicated by the straight line. This was done by maximising the likelihood, assuming that $\ln \rho$ has a Gaussian distribution with standard deviation derived from the scatter of points. The SNR shows no clear correlation with the other parameters; the mass-scaling successfully removes any dependence upon μ . However, the SNR is sensitive to the intrinsic parameters, in particular the initial position (as this determines the subsequent trajectory), and may vary by an order of magnitude.

The parameter uncertainties are well correlated with the SNR. The uncertainties are plotted against SNR in Fig. 7.2. We have now plotted the entire data set, and not just the averaged points, to give an indication of the spread. Some uncertainties show a dependence upon the MBH spin or the orbital inclination.

The uncertainty for the majority of parameters seem to be reasonably well described by a simple power-law. This is fitted, as for the SNR-periapsis relation, using maximum likelihood, assuming that $\ln \rho$ and $\ln \sigma_a$ have independent Gaussian distributions with standard deviations derived from the scatter of points. This is not the case: since we are only interested in quantifying the general trend to give a broad estimate of the behaviour, we shall not be concerned by the error introduced here.⁶ The fitted parameters are given in Table 1.

For small SNRs, the Fisher matrix is no longer an appropriate estimate for the inverse covariance matrix; this only hold in the limit of high SNR Vallisneri (2008). Therefore we should not expect these results to hold for low SNRs. However, we are unlikely to detect these signals in practise, so this is not a significant concern.

The uncertainty in the MBH mass and in the GC distance show a clear kink, and are better fit by a broken power-law. Above the break, higher SNRs give diminished returns.

⁶ A basic least-squares fit yields similar results.

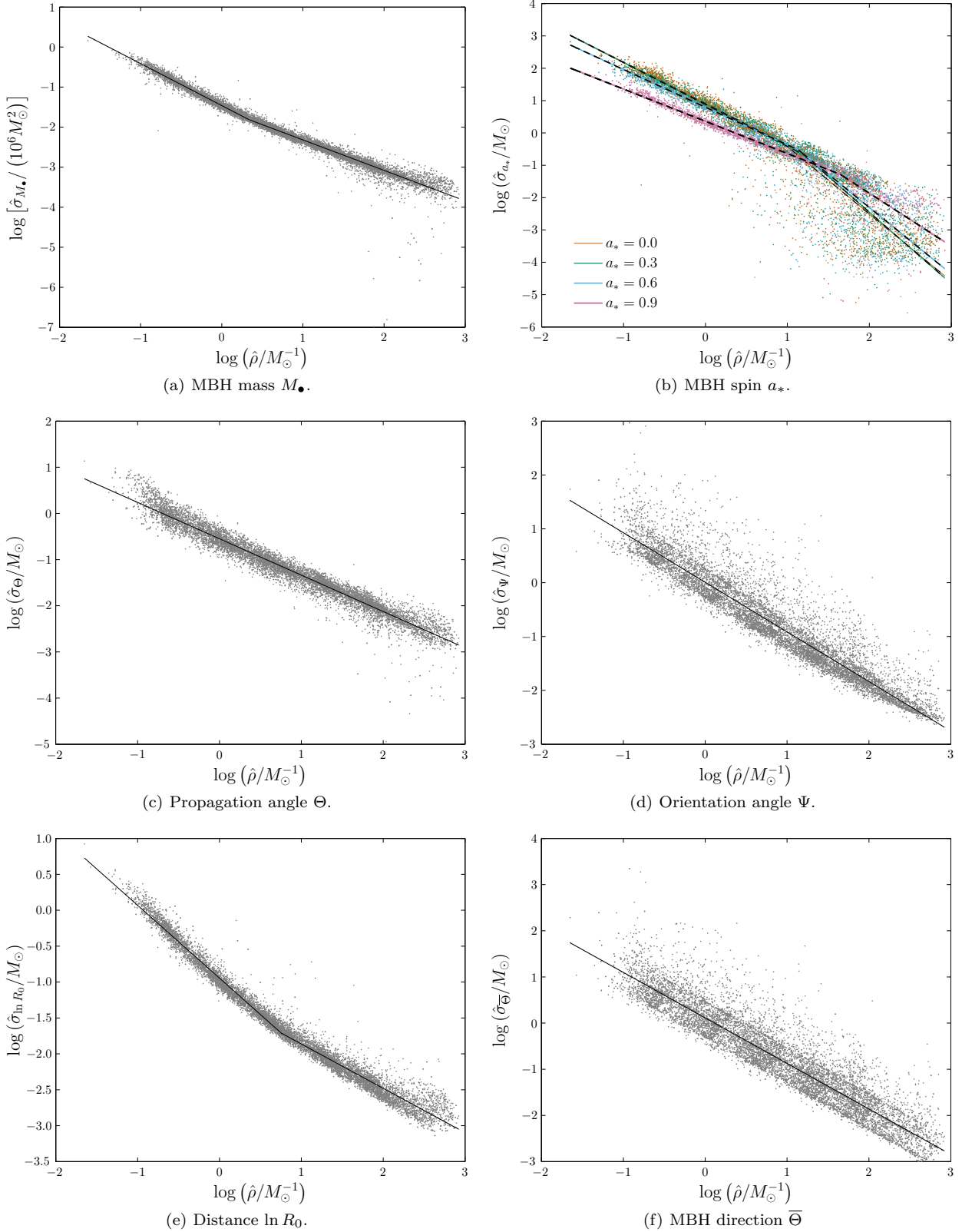


Figure 9. Mass-normalised parameter uncertainties and SNR. The points represent the entire set of data. The lines are maximum likelihood fits to the values obtained by averaging over each set of intrinsic parameters. See Table 1 for best fit parameters.

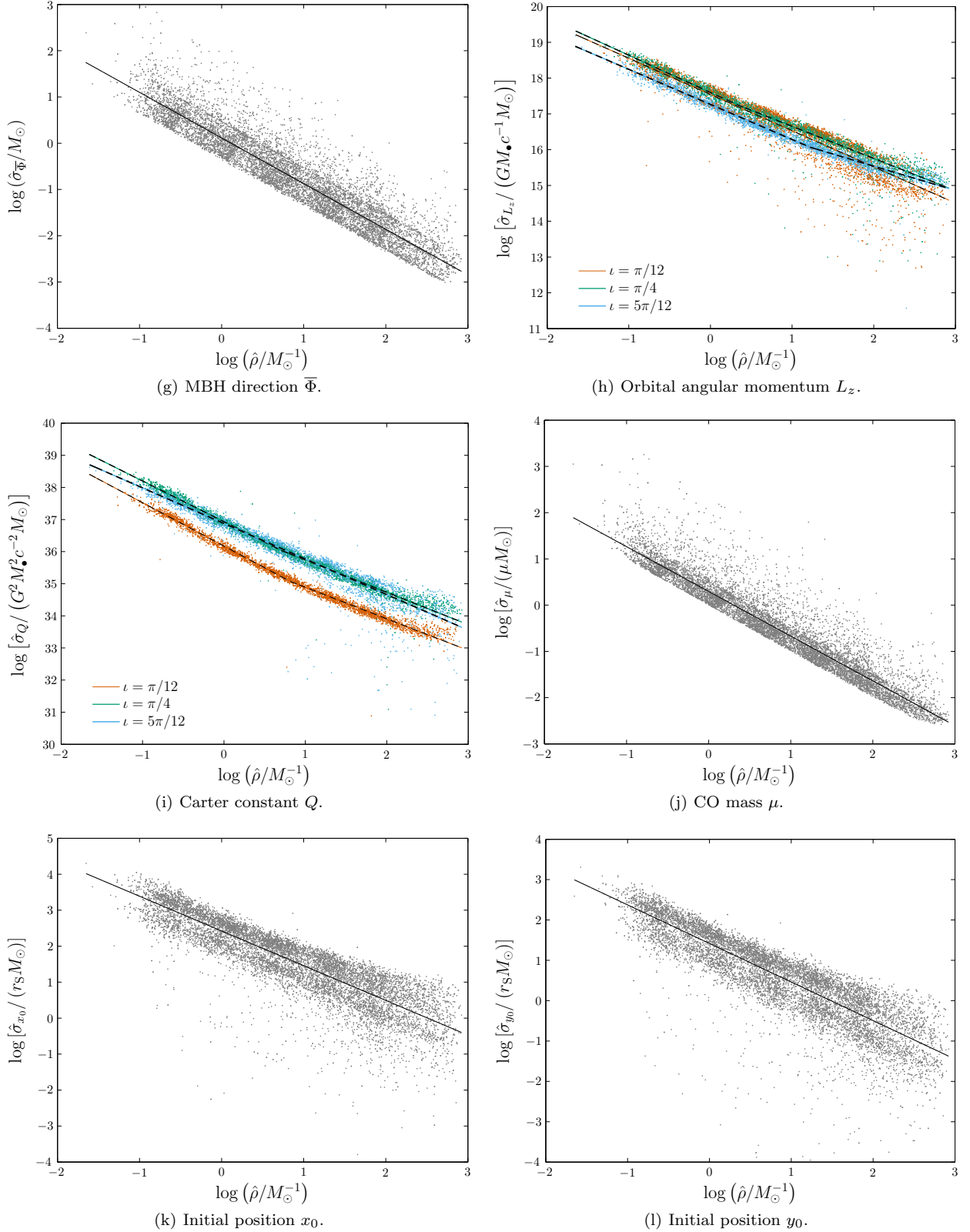


Figure 9 – continued Mass-normalised parameter uncertainties and SNR. The points represent the entire set of data. The lines are maximum likelihood fits to the values obtained by averaging over each set of intrinsic parameters. See Table 1 for best fit parameters.

Table 1. Best fit parameters for power-laws of the form $\log(\Xi) = A \log\left(\hat{\rho}/M_{\odot}^{-1}\right) + B$. For broken power-laws a pair of values for A and B are given. The reduced chi-squared value χ^2/ν was not used for fitting, as the standard deviation included in the likelihood varies with A , but is included as a goodness-of-fit statistic.

Ξ	Extrinsic parameter	A_1	B_1	A_2	B_2	χ^2/ν
$\hat{\sigma}_{M_{\bullet}}/(10^6 M_{\odot}^2)$	–	–1.05	–1.46	–0.76	–1.56	0.29
$\hat{\sigma}_{a_*}/M_{\odot}$	$a_* = 0.0$	–1.28	0.91	–2.08	1.66	2.06
	$a_* = 0.3$	–1.29	0.88	–2.21	1.97	1.70
	$a_* = 0.6$	–1.16	0.80	–2.06	1.81	1.46
	$a_* = 0.9$	–1.00	0.36	–1.64	1.42	0.85
$\hat{\sigma}_{\Theta}/M_{\odot}$	–	–0.79	–0.55	–	–	1.30
$\hat{\sigma}_{\Psi}/M_{\odot}$	–	–0.92	0.01	–	–	0.73
$\hat{\sigma}_{\ln R_0}/M_{\odot}$	–	–1.01	–0.94	–0.62	–1.24	0.46
$\hat{\sigma}_{\overline{\Theta}}/M_{\odot}$	–	–0.99	0.11	–	–	0.75
$\hat{\sigma}_{\overline{\Phi}}/M_{\odot}$	–	–0.99	0.11	–	–	0.75
$\hat{\sigma}_{L_z}/(GM_{\bullet}c^{-1}M_{\odot})$	$\iota = \pi/12$	–1.01	17.54	–	–	5.39
	$\iota = \pi/4$	–1.06	17.60	–0.90	17.55	1.12
	$\iota = 5\pi/12$	–0.98	17.26	–0.68	16.90	0.23
$\hat{\sigma}_Q/(G^2 M_{\bullet}^2 c^{-2} M_{\odot})$	$\iota = \pi/12$	–1.35	36.17	–0.98	35.87	0.26
	$\iota = \pi/4$	–1.27	36.93	–1.01	36.75	0.25
	$\iota = 5\pi/12$	–1.11	36.88	–	–	1.06
$\hat{\sigma}_{\mu}/(\mu M_{\odot})$	–	–0.97	0.30	–	–	0.60
$\hat{\sigma}_{x_0}/(r_S M_{\odot})$	–	–0.97	1.42	–	–	1.11
$\hat{\sigma}_{y_0}/(r_S M_{\odot})$	–	–0.96	1.42	–	–	1.08
$\hat{\sigma}_{z_0}/(r_S M_{\odot})$	$\iota = \pi/12$	–0.94	1.89	–0.72	1.70	0.27
	$\iota = \pi/4$	–0.80	1.72	–	–	0.41
	$\iota = 5\pi/12$	–0.77	1.43	–	–	0.70

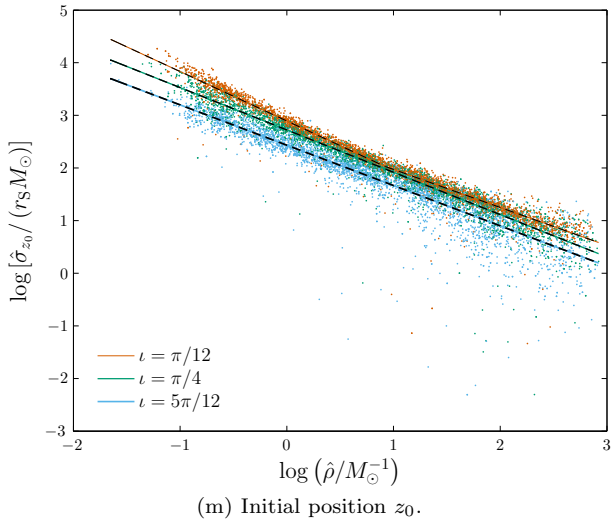


Figure 9 – continued Mass-normalised parameter uncertainties and SNR. The points represent the entire set of data. The lines are maximum likelihood fits to the values obtained by averaging over each set of intrinsic parameters. See Table 1 for best fit parameters.

A broken power-law does not improve the fit of any of the other uncertainties which only depend upon the SNR.

The fits for x_0 and y_0 , and for $\overline{\Theta}$ and $\overline{\Phi}$ are practically identical. In both cases the variables are physically similar.

Unsurprisingly, the uncertainty in the spin depends upon the spin parameter. Larger values of a_* give smaller uncertainties: at the same periapse radius a larger spin parameter would have a greater impact on the spacetime, and thus the orbit. However, σ_a is not well approximated by

power law for small periapses (large SNR), as is evident from the large spread in values. We have fitted a broken law in lieu of a better model: the piece for lower SNR gives a reasonable indication of the behaviour, however the other piece is not to be trusted. The break gives an indication of where the simple power law approximation is no longer applicable. The complicated behaviour reflects the intricate dependence of the shape of the trajectory, which determines the waveform, upon the orbital parameters, including the initial position, as well as the background spacetime. There is more scatter for smaller a_* , perhaps reflecting that a small change in a small spin parameter has a greater impact on the trajectory than a small change in a large spin parameter.

The orbital inclination influences σ_{L_z} , σ_Q and σ_{z_0} . The first two are easily understood, since the inclination determines the value of the two components of angular momenta for a given r_p . The dependence in σ_{z_0} can be explained by considering motion out of the equatorial plane: this is determined by the inclination, which sets the momentum out of the plane, and the initial position, which specifies the trajectory.

The uncertainties in L_z and Q show opposite dependencies upon ι . This antagonistic behaviour occurs because a low inclination means small Q and large L_z relative to L_{∞} , while a high inclination means the reverse. Both quantities have smaller uncertainties when they are smaller themselves, suggesting we may be measuring something akin to fractional changes in the angular momenta: this cannot be exactly the case, since Q can be zero, and L_z may be negative. There is a larger spread in the uncertainties at small periapses when the quantities are larger. This again reflects the fact that these orbits may have complicated shapes that can vary significantly with a change in the orbital parameters; when either L_z or Q is the dominant component of

L_∞ , it plays the more significant role in determining the trajectory, and changing the other has only a small impact. This large scatter means that a power-law is not a good fit for these inclinations at high SNR, and we must be cautious extrapolating results.

A broken power-law better fits $\hat{\sigma}_{L_z}$ for $\iota = 5\pi/12$ and $\pi/4$, and $\hat{\sigma}_Q$ for $\iota = \pi/12$ and $\pi/4$. In both cases the change in gradient for the $\iota = \pi/4$ case is slight.

The uncertainty in z_0 is smaller for larger inclinations, as then we have greater motion out of the equatorial plane. A broken power-law is a better fit for both $\iota = \pi/12$.

Only the spin and inclination appear to influence the SNR-uncertainty relations. The mass-normalisation removes any dependence of mass, however we have considered $\hat{\sigma}_\mu/\mu$ to ensure this. There is no obvious dependence upon the sense of rotation; we would expect this to most influence σ_a for orbits with very small periapses, since it is the spin that induces a difference between orbits of opposite senses and this effect is only noticeable close to the MBH. Since there is significant scatter in values of σ_a for small periapses, it is unsurprising that we have not noticed any dependence upon the rotation sense, if it were present.

7.3 Comparison with existing results

Having quantified the accuracy with which we could hope to infer parameters from an EMRB waveform, we can now compare these results with existing measurements, to see if it is possible to learn anything new.

We have no *a priori* knowledge about the CO, or its orbit, so anything we can deduce about its initial position, angular momentum or mass would be new. Measurements of the mass are only useful if σ_μ/μ is less than 1. Form our power law, this would occur for a $1.4M_\odot$ ($10M_\odot$) object when $\rho \simeq 2.00$ (1.88). Since we would only expect to detect signals with SNRs of order of a few, we conclude that any detectable signal will give us some constraint on the compact object's mass. An uncertainty of 10% would be possible for $\rho \simeq 21.7$ (20.2).

Similarly, we have no information on the orientation of the MBH, so any measurement for which σ_Θ or σ_Ψ is less than 2π would be of interest. This happens for very low SNR for both angles, so again a detection would allow us to infer something new. An uncertainty of $\pi/72 = 5$ deg corresponds to $\rho \simeq 9.78$ (5.76) for Θ and $\rho \simeq 29.6$ (25.1) for Ψ .

We have existing measurements for the position of the MBH. The current constraints on $\bar{\Theta}$ and $\bar{\Phi}$ cannot be matched by observing EMRBs. The uncertainty in $\ln R_0$ based on existing measurements is $\sigma_{\ln R_0}^0 \simeq 0.042$. This could be bettered by an EMRB with $\rho \simeq 2.68$ (2.75).

Of paramount interest are the MBH mass and spin. The current uncertainty in the mass is $\sigma_{M_\bullet}^0 = 0.36 \times 10^6 M_\odot$. This can be equalled for very low SNR, $\rho \simeq 0.11$ (0.12), so any detection should be able to improve measurement for M_\bullet . A 0.1% accuracy could be obtained for $\rho \approx 10.4$ (8.11).

The spin is less well known. To obtain an uncertainty of 0.1 would require $\rho \sim 23$ ($\simeq 51.1$) for $a_* = 0.0$; $\rho \sim 27$ ($\simeq 47.9$) for $a_* = 0.3$; $\rho \sim 28$ ($\simeq 48.3$) for $a_* = 0.6$, and $\rho \simeq 23.1$ ($\simeq 23.0$) for $a_* = 0.9$. We have used \sim to denote values obtained using the higher SNR piece of the power-law, these values are much less accurate because of the large degree of scatter.

8 ENERGY SPECTRA

To check that the NK waveforms are sensible, we may compare the energy spectra calculated from these with those obtained from the classic treatment of Peters & Mathews (1963), and Peters (1964). This calculates GW emission for Keplerian orbits in flat spacetime, assuming only quadrupole radiation. The spectrum produced should be similar to that obtained from the NK in weak fields, that is for orbits with a large periapsis; however we do not expect an exact match because of the differing input physics and various approximations.

In addition to using the energy spectrum, we can also use the total energy flux to check the NK waveforms. The total flux contains less information than the spectrum; however results have been calculated for parabolic orbits in Schwarzschild spacetime using time-domain black hole perturbation theory (Martel 2004). These should be more accurate than results calculated using the Peters and Mathews formalism.

We do not intend to use the kludge waveforms to calculate an accurate energy flux: this would be inconsistent as we assume that the orbits do not evolve with time. We only calculate the energy flux as a sanity check, to confirm that the kludge approximation is consistent with other approaches.

8.1 Kludge spectrum

A gravitational wave in the TT gauge has an effective energy-momentum tensor (Misner et al. 1973, section 35.15)

$$T_{\mu\nu} = \frac{c^4}{32\pi G} \left\langle \partial_\mu h_{ij} \partial_\nu h^{ij} \right\rangle, \quad (56)$$

where $\langle \dots \rangle$ indicates averaging over several wavelengths or periods. The flux of energy through a sphere of radius $r = R$ is

$$\frac{dE}{dt} = \frac{c^3}{32\pi G} R^2 \int d\Omega \left\langle \frac{dh_{ij}}{dt} \frac{dh^{ij}}{dt} \right\rangle, \quad (57)$$

with $\int d\Omega$ representing integration over all solid angles. From (26) we see that the waves have a $1/r$ dependence; if we define

$$h_{ij} = \frac{H_{ij}}{r}, \quad (58)$$

we see that, using (26), the flux is independent of R , as required for energy conservation, and

$$\frac{dE}{dt} = \frac{c^3}{32\pi G} \int d\Omega \left\langle \frac{dH_{ij}}{dt} \frac{dH^{ij}}{dt} \right\rangle. \quad (59)$$

If we now integrate to find the total energy emitted we obtain

$$E = \frac{c^3}{32\pi G} \int d\Omega \int_{-\infty}^{\infty} dt \frac{dH_{ij}}{dt} \frac{dH^{ij}}{dt}. \quad (60)$$

Since we are considering all time, the localization of the energy is no longer of importance and it is unnecessary to average over several periods. Switching to Fourier representation $\tilde{H}_{ij}(f) = \mathcal{F}\{H_{ij}(t)\}$,

$$E = \frac{\pi c^3}{4G} \int d\Omega \int_0^{\infty} df f^2 \tilde{H}^{ij}(f) \tilde{H}_{ij}^*(f), \quad (61)$$

using the fact that the signal is real so $\tilde{H}_{ij}^*(f) = \tilde{H}_{ij}(-f)$. From this we identify the energy spectrum as

$$\frac{dE}{df} = \frac{\pi c^3}{4G} \int d\Omega f^2 \tilde{H}^{ij}(f) \tilde{H}_{ij}^*(f). \quad (62)$$

8.2 Peters and Mathews spectrum

To calculate the Peters and Mathews energy spectrum for a parabolic orbit, we use the limiting result of Turner (1977)

$$\begin{aligned} \frac{dE}{df} = & \frac{4\pi^2}{5} \frac{G^3}{c^5} \frac{M_\bullet \mu^2}{r_p^2} \left\{ \left[\frac{8f^2}{f_c^2} B\left(\frac{f}{f_c}\right) - \frac{2f}{f_c} A\left(\frac{f}{f_c}\right) \right]^2 \right. \\ & \left. + \left(\frac{128f^4}{f_c^4} + \frac{4f^2}{3f_c^2} \right) \left[A\left(\frac{f}{f_c}\right) \right]^2 \right\}, \end{aligned} \quad (63)$$

where f_c is the orbital frequency of a circular orbit of radius equal to r_p ,

$$f_c = \frac{1}{2\pi} \sqrt{\frac{G(M_\bullet + \mu)}{r_p^3}}, \quad (64)$$

and functions $A(x)$ and $B(x)$ are defined in terms of Bessel functions. Their precise forms are (Berry & Gair 2010)

$$A(x) = \frac{1}{\pi} \sqrt{\frac{2}{3}} K_{1/3} \left(\frac{2^{3/2}x}{3} \right); \quad (65)$$

$$\begin{aligned} B(x) = & \frac{1}{\sqrt{3}\pi} \left[K_{-2/3} \left(\frac{2^{3/2}x}{3} \right) + K_{4/3} \left(\frac{2^{3/2}x}{3} \right) \right. \\ & \left. - \frac{1}{\sqrt{2}x} K_{1/3} \left(\frac{2^{3/2}x}{3} \right) \right], \end{aligned} \quad (66)$$

where $K_\nu(z)$ is a modified Bessel function of the second kind. This result should be accurate to $\sim 10\%$ for orbits with periapse radii larger than $\sim 10r_s$, where r_s is the MBH's Schwarzschild radius (Berry & Gair 2010).

8.3 Comparison

Two energy spectra are plotted in Fig. 10 for orbits with periapses of $r_p = 7.5r_s$, $15.0r_s$ and $30.0r_s$. The two spectra appear to be in good agreement, showing the same general shape in the weak-field limit. The NK spectrum is more tightly peaked, but is always within a factor of 2 at the apex. The peak of the spectrum is shifted to a marginally higher frequency in the NK spectrum because of the contribution for the current quadrupole and mass octupole terms.

Comparing the total energy fluxes, ratios of the various energies are plotted in Fig. 11. We introduce an additional energy here, the quadrupole NK energy $E_{NK(Q)}$. This allows easier comparison with the Peters and Mathews energy which is calculated assuming only quadrupole radiation. It can be calculated in three ways:

(i) Inserting the waveform $\tilde{h}(f)$ generated including only the mass quadrupole term in (26) into (61) and integrating. This is equivalent to the method used to calculate E_{NK} .

(ii) Numerically integrating the quadrupole GW luminosity (Misner et al. 1973, section 36.7; Hobson et al. 2006, section 18.7)

$$E = \frac{G}{5c^9} \int \ddot{I}_{ij} \ddot{I}^{ij} dt, \quad (67)$$

where $I_{ij} = I_{ij} - (1/3)I\delta_{ij}$ is the reduced mass quadrupole tensor. We can obtain this from (60), by integrating over all angles when the waveform only contains the mass quadrupole component. This has the advantage of avoiding the effects of spectral leakage or the influence of window functions.

(iii) Using the analytic expressions for the integral (67) given in appendix A of Gair et al. (2005).

All three agree to within computational error. This demonstrates the validity of the code, and shows that the use of a window function does not significantly distort the waveform.

The ratios all tend towards one in the weak field, as required, but differences become more pronounced in the strong field. The NK energy is larger than the Peters and Mathews result E_{PM} : since this only assumes quadrupole radiation, we have only plotted it against $E_{NK(Q)}$. This behaviour has been seen before for high eccentricity orbits about a non-spinning BH (Gair et al. 2005). It may be explained by considering the total amount of rotation for the different orbits: the Peters and Mathews spectrum assumes a Keplerian orbit, so the total rotation is $\Delta\phi = 2\pi$; the orbit in Kerr geometry rotates more than this (the angle would be 2π in the limit of an infinite periapsis, whereas for a periapsis small enough that the orbit shows zoom-whirl behaviour, the total angle may be many times 2π). The greater rotation leads to increased emission of gravitational waves and a larger energy flux (Berry & Gair 2010). As expected, there appears to be reasonable correlation between the amount of rotation $2\pi/\Delta\phi$ and the ratio of energies.

Error in the NK energy compared with the time-domain black hole perturbation theory results of Martel comes from two sources: the neglecting of higher order multipole contributions and the ignoring of background curvature. The contribution of the former can be estimated by looking at the difference in the NK energy by including the current quadrupole and mass octupole terms. From Fig. 11 we see that these terms give a negligible contribution in the weak field, but the difference is $\sim 20\%$ in the strong field. This explains why the Martel energy E_M is greater in the strong field, as it includes contributions from all multipoles. Neglecting the background curvature increases the NK energy relative to E_M . This partially cancels out the error introduced by not including higher order terms: this accidentally leads to $E_{NK(Q)}$ being more accurate than E_{NK} for $r_p \gtrsim 5r_s$ (Tanaka et al. 1993).

From the level of agreement we may be confident that the NK waveforms are a reasonable approximation. The difference in energy flux is only greater than 10% for very strong fields $r_p \simeq 2r_s$; since this is dependent on the square of the waveform, typical accuracy in the waveform may be $\sim 5\%$ (Gair et al. 2005; Tanaka et al. 1993).

9 DISCUSSION

We have outlined an approximate method of generating gravitational waveforms for EMRBs originating at the GC. This assumes that the orbits are parabolic and employs a numerical kludge approximation. The two coordinate schemes for a NK presented here yield almost indistinguishable results. We conclude that either is a valid choice for this purpose.

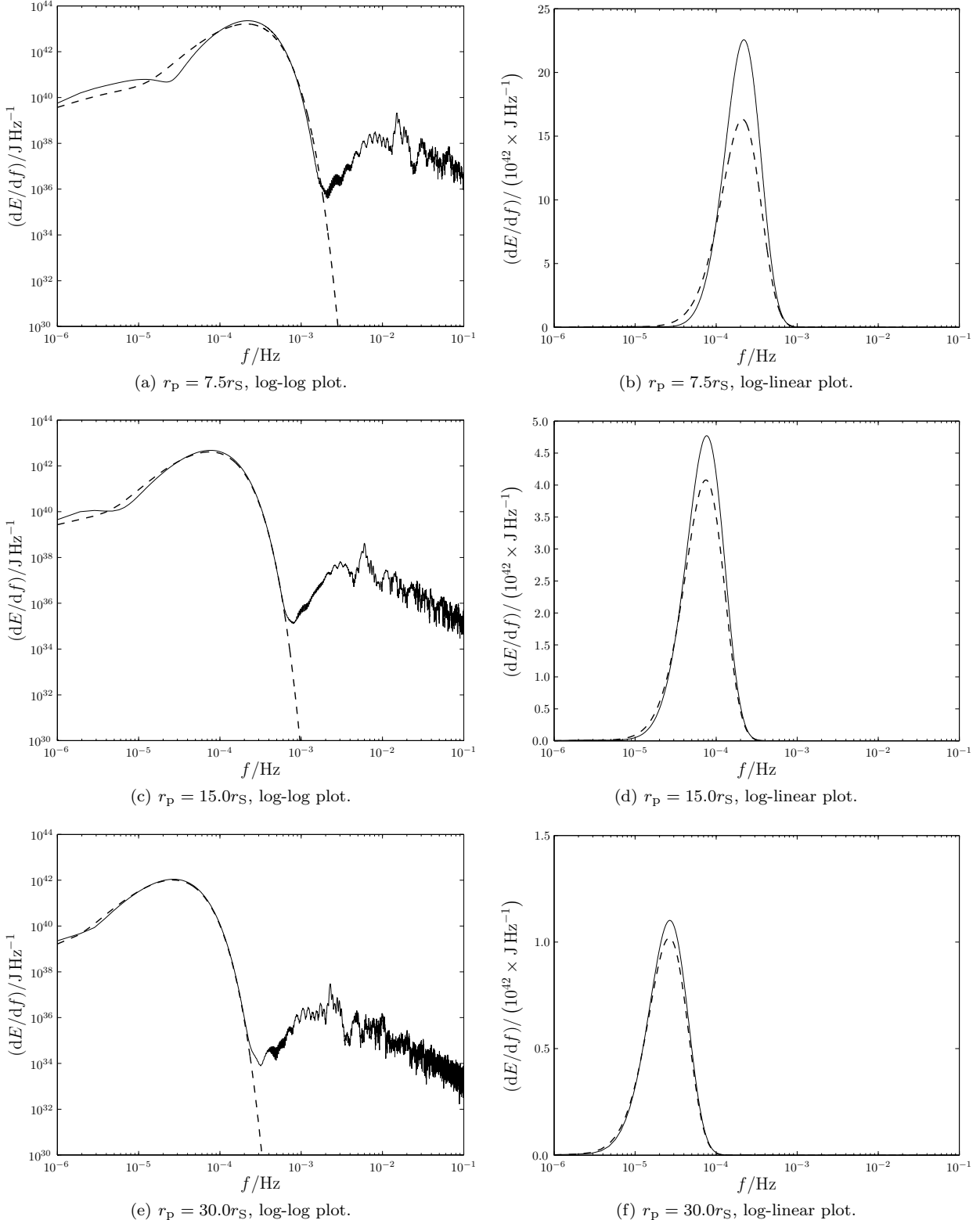


Figure 10. Energy spectra for a parabolic orbit of a $\mu = 10M_\odot$ object about a Schwarzschild BH with $M_\bullet = 4.31 \times 10^6 M_\odot$. The spectra calculated from the NK waveform is shown by the solid line and the Peters and Mathews flux is indicated by the dashed line. The NK waveform includes octupole contributions. The high frequency tail is the result of spectral leakage.

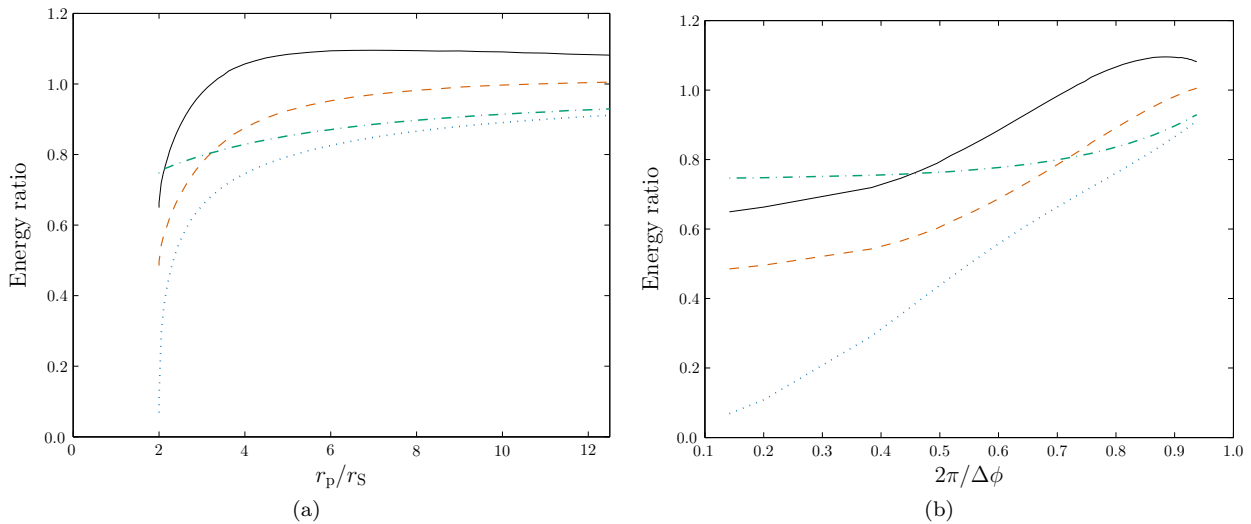


Figure 11. Ratios of energies as a function of periapsis r_p and 2π divided by the total angle of rotation in one orbit $\Delta\phi$ ($2\pi/\Delta\phi = 1$ for a Keplerian orbit). The solid line shows the ratio of the numerical kludge and Martel energies E_{NK}/E_M ; the dashed line shows the ratio of the NK energy calculated using only the mass quadrupole term and the Martel energy $E_{NK(Q)}/E_M$; the dot-dashed line shows the ratio of the quadrupole and quadrupole-octupole NK energies $E_{NK(Q)}/E_{NK}$, and the dotted line shows the ratio of the Peters and Mathews and quadrupole NK energies $E_{PM}/E_{NK(Q)}$. Compare with figure 4 of Gair et al. (2005).

The waveforms created appear to be consistent with results obtained using Peters and Mathews waveforms for large periapses, indicating that they have the correct weak-field form. The NK approach should be superior to that of Peters and Mathews in the strong-field regime as it uses the exact geodesics of the Kerr spacetime.

Using the NK waveforms we have conducted a trial investigation, using Fisher matrix analysis, into how accurately we could infer parameters of the galactic centre's MBH should such an EMRB be observed. Potentially, it is possible to determine very precisely the key parameters defining the MBH's mass and spin, if the orbit gets close enough to the black hole.

From our investigation it appears that we can achieve good results from a single EMRB with periapsis of $r_p = 50M_\bullet$. This translates to a distance of 10^{11} m or 10^{-5} pc.

Before we can quote results for how accurately we can determine the various parameters, we must consider the probability of each orbit. This will be the subject of a future paper, building upon the earlier results of Rubbo et al. (2006) and Hopman et al. (2007), who only considered the probability for a signal to be detectable. Using a model for the galactic centre it is possible to define distributions for angular momenta L_z and Q , for a species of mass μ . With these it is possible to estimate the event rate, and define an expectation value for the elements of the variance-covariance matrix Σ . This would describe how much information, on average, we could hope to obtain from EMRB observations.

Some consideration should also be given to methods of fitting a waveform to an observed signal. Given an input signal, what is the best algorithm for finding the optimal set of parameters to characterise the observed waveform? It is necessary to consider this to check if there are degenerate combinations of parameters that produce similar waveforms; a first step would be to consider the off-diagonal terms of the inverse Fisher matrix with give parameter cor-

relations. For example there is a large degeneracy between the GC distance and the compact object mass, fortunately this can be mitigated through the use of prior knowledge of R_0 . However, if there are degenerate regions sufficiently distinct in parameter space we would not be aware of them by only considering the region immediately about the ML point and a Fisher matrix analysis is insufficient. In this work we have assumed that we can correctly identify the waveform's parameters. We do not intend to use NK waveforms to actually identify real GWs: more accurate methods should be employed for that; the point of this study would be to identify potential pitfalls that could be encountered when using accurate waveforms.

We have shown that the uncertainties in the maximum likelihood parameters as obtained from a Fisher matrix analysis are correlated with the SNR. In most cases they may be approximated as simple power laws, although this does not encapsulate the full richness of phenomenology, and may break down at small periapses, most notably for the spin parameter. The dependence on compact object mass can easily be removed by scaling.

We could extend the simple Fisher matrix analysis performed here to a full Bayesian analysis with the distributions for L_z , Q , μ , x_0 , y_0 and z_0 serving as priors. However this may be too computationally expensive to justify implementing.

A natural continuation of this work would be to consider EMRBs from other MBHs. LISA should be able to detect EMRBs originating from the Virgo cluster (Rubbo et al. 2006), however the detectable rate may be only 10^{-4} yr $^{-1}$ per galaxy (Hopman et al. 2007). It would be interesting to check what we could expect to infer about MBHs in other galaxies from GWs.

REFERENCES

- Amaro-Seoane P., Gair J. R., Freitag M., Miller M. C., Mandel I., Cutler C. J., Babak S., 2007, Classical and Quantum Gravity, 24, R113
- Babak S., Fang H., Gair J., Glampedakis K., Hughes S., 2007, Physical Review D, 75, 024005
- Backer D. C., Sramek R. A., 1999, The Astrophysical Journal, 524, 805
- Barack L., Cutler C., 2004, Physical Review D, 69, 082005
- Bekenstein J. D., 1973, The Astrophysical Journal, 183, 657
- Bélanger G., Terrier R., de Jager O. C., Goldwurm A., Melia F., 2006, Journal of Physics: Conference Series, 54, 420
- Bender P., Brillet A., Ciufolini I., Cruise A. M., Cutler C., Danzmann K., 1998, Technical report, LISA Pre-Phase A Report. Max-Planck-Institut für Quantenoptik, Garching
- Berry C. P. L., Gair J. R., 2010, Physical Review D, 82, 107501
- Berti E., Cardoso V., Gonzalez J. A., Sperhake U., Hannam M., Husa S., Brügmann B., 2007, Physical Review D, 76, 064034
- Berti E., Volonteri M., 2008, The Astrophysical Journal, 684, 822
- Boyer R. H., Lindquist R. W., 1967, Journal of Mathematical Physics, 8, 265
- Brenneman L. W., Reynolds C. S., 2006, The Astrophysical Journal, 652, 1028
- Burko L. M., Khanna G., 2007, EPL, 78, 60005
- Carter B., 1968, Physical Review, 174, 1559
- Carter B., 1971, Physical Review Letters, 26, 331
- Chandrasekhar S., 1998, The Mathematical Theory of Black Holes. Oxford Classic Texts in the Physical Sciences, Oxford University Press, Oxford
- Cutler C., 1998, Physical Review D, 57, 7089
- Cutler C., Flanagan E. E., 1994, Physical Review D, 49, 2658
- Damour T., Iyer B. R., Sathyaprakash B. S., 2000, Physical Review D, 62, 084036
- Danzmann K., Rüdiger A., 2003, Classical and Quantum Gravity, 20, S1
- de Felice F., 1980, Journal of Physics A: Mathematical and General, 13, 1701
- de la Calle Pérez I., Longinotti A. L., Guainazzi M., Bianchi S., Dovčiak M., Cappi M., Matt G., Miniutti G., Petrucci P. O., Piconcelli E., Ponti G., Porquet D., Santos-Lleo M., 2010, Astronomy & Astrophysics, 524, A50
- Doeleman S. S., Weintraub J., Rogers A. E. E., Plambeck R., Freund R., 2008, Nature, 455, 78
- Drasco S., Hughes S., 2004, Physical Review D, 69, 044015
- Ferrarese L., Merritt D., 2000, The Astrophysical Journal, 539, L9
- Finn L. S., 1992, Physical Review D, 46, 5236
- Gair J. R., Kennefick D. J., Larson S. L., 2005, Physical Review D, 72, 084009
- Gammie C. F., Shapiro S. L., McKinney J. C., 2004, The Astrophysical Journal, 602, 312
- Gebhardt K., Bender R., Bower G., Dressler A., Faber S. M., Filippenko A. V., Green R., Grillmair C., Ho L. C., Kormendy J., Lauer T. R., Magorrian J., Pinkney J., Richstone D., Tremaine S., 2000, The Astrophysical Journal, 539, L13
- Genzel R., Schödel R., Ott T., Eckart A., Alexander T., Lacombe F., Rouan D., Aschenbach B., 2003, Nature, 425, 934
- Ghez A. M., Salim S., Weinberg N. N., Lu J. R., Do T., Dunn J. K., Matthews K., Morris M. R., Yelda S., Becklin E. E., Kremenek T., Milosavljevic M., Naiman J., 2008, The Astrophysical Journal, 689, 1044
- Gillessen S., Eisenhauer F., Trippe S., Alexander T., Genzel R., Martins F., Ott T., 2009, The Astrophysical Journal, 692, 1075
- Glampedakis K., 2005, Classical and Quantum Gravity, 22, S605
- Glampedakis K., Hughes S., Kennefick D., 2002, Physical Review D, 66, 064005
- Glampedakis K., Kennefick D., 2002, Physical Review D, 66, 044002
- González J. A., Sperhake U., Brügmann B., Hannam M., Husa S., 2007, Physical Review Letters, 98, 091101
- Graham A. W., 2007, Monthly Notices of the Royal Astronomical Society, 379, 711
- Graham A. W., Erwin P., Caon N., Trujillo I., 2001, The Astrophysical Journal, 563, L11
- Graham A. W., Onken C. A., Athanassoula E., Combes F., 2011, Monthly Notices of the Royal Astronomical Society, 412, 2211
- Haiman Z., Quataert E., 2004, The Formation and Evolution of the First Massive Black Holes. Kluwer Academic Publishers, Dordrecht, pp 147–186
- Hamaus N., Paumard T., Müller T., Gillessen S., Eisenhauer F., Trippe S., Genzel R., 2009, The Astrophysical Journal, 692, 902
- Häring N., Rix H.-W., 2004, The Astrophysical Journal, 604, L89
- Harris F., 1978, Proceedings of the IEEE, 66, 51
- Hawking S. W., 1972, Communications in Mathematical Physics, 25, 152
- Hobson M. P., Efstathiou G., Lasenby A., 2006, General Relativity: An Introduction for Physicists. Cambridge University Press, Cambridge
- Hopman C., Freitag M., Larson S. L., 2007, Monthly Notices of the Royal Astronomical Society, 378, 129
- Hughes S. A., Blandford R. D., 2003, The Astrophysical Journal, 585, L101
- Israel W., 1967, Physical Review, 164, 1776
- Israel W., 1968, Communications in Mathematical Physics, 8, 245
- Jaynes E. T., 2003, Probability Theory: The Logic of Science. Cambridge University Press, Cambridge
- Kaiser J., Schafer R., 1980, Acoustics, Speech and Signal Processing, IEEE Transactions on, 28, 105
- Kato Y., Miyoshi M., Takahashi R., Negoro H., Matsumoto R., 2010, Monthly Notices of the Royal Astronomical Society: Letters, 403, L74
- Kerr R., 1963, Physical Review Letters, 11, 237
- King A. R., Pringle J. E., 2006, Monthly Notices of the Royal Astronomical Society: Letters, 373, L90
- King A. R., Pringle J. E., Hofmann J. A., 2008, Monthly Notices of the Royal Astronomical Society, 385, 1621
- Kormendy J., Richstone D., 1995, Annual Review of Astronomy and Astrophysics, 33, 581
- Larson S. L., Hellings R. W., Hiscock W. A., 2002, Physical

- Review D, 66, 062001
- Larson S. L., Hiscock W. A., Hellings R. W., 2000, Physical Review D, 62, 062001
- Lynden-Bell D., Rees M. J., 1971, Monthly Notices of the Royal Astronomical Society, 152, 461
- McClintock J. E., Narayan R., Davis S. W., Gou L., Kulkarni A., Orosz J. A., Penna R. F., Remillard R. A., Steiner J. F., 2011, Classical and Quantum Gravity, 28, 114009
- MacKay D. J. C., 2003, Information Theory, Inference and Learning Algorithms. Cambridge University Press, Cambridge
- McKeehan D. J. A., Robinson C., Sathyaprakash B. S., 2010, Classical and Quantum Gravity, 27, 084020
- Magorrian J., Tremaine S., Richstone D., Bender R., Bower G., Dressler A., Faber S. M., Gebhardt K., Green R., Grillmair C., Kormendy J., Lauer T., 1998, The Astronomical Journal, 115, 2285
- Malbon R. K., Baugh C. M., Frenk C. S., Lacey C. G., 2007, Monthly Notices of the Royal Astronomical Society, 382, 1394
- Marconi A., Hunt L. K., 2003, The Astrophysical Journal, 589, L21
- Martel K., 2004, Physical Review D, 69, 044025
- Merritt D., Alexander T., Mikkola S., Will C. M., 2010, Physical Review D, 81, 062002
- Miller J., 2007, Annual Review of Astronomy and Astrophysics, 45, 441
- Miniutti G., Panessa F., De Rosa A., Fabian A. C., Malizia A., Molina M., Miller J. M., Vaughan S., 2009, Monthly Notices of the Royal Astronomical Society, 398, 255
- Misner C. W., Thorne K. S., Wheeler J. A., 1973, Gravitation. W. H. Freeman, New York
- Nardini E., Fabian A. C., Reis R. C., Walton D. J., 2011, Monthly Notices of the Royal Astronomical Society, 410, 1251
- Nuttall A., 1981, IEEE Transactions on Acoustics, Speech and Signal Processing, 29, 84
- Patrick A. R., Reeves J. N., Porquet D., Markowitz A. G., Lobban A. P., Terashima Y., 2011, Monthly Notices of the Royal Astronomical Society, 411, 2353
- Peters P. C., 1964, Physical Review, 136, B1224
- Peters P. C., Mathews J., 1963, Physical Review, 131, 435
- Press W., 1977, Physical Review D, 15, 965
- Psaltis D., 2008, Living Reviews in Relativity, 11
- Rees M. J., 1984, Annual Review of Astronomy and Astrophysics, 22, 471
- Reid M. J., Menten K. M., Genzel R., Ott T., Schödel R., Brunthaler A., 2003, Astronomische Nachrichten, 324, 505
- Reid M. J., Readhead A. C. S., Vermeulen R. C., Treuhaft R. N., 1999, The Astrophysical Journal, 524, 816
- Robinson D., 1975, Physical Review Letters, 34, 905
- Rosquist K., Bylund T., Samuelsson L., 2009, International Journal of Modern Physics D, 18, 429
- Rubbo L. J., Holley-Bockelmann K., Finn L. S., 2006, The Astrophysical Journal, 649, L25
- Ruffini R., Sasaki M., 1981, Progress of Theoretical Physics, 66, 1627
- Sathyaprakash B., Schutz B. F., 2009, Living Reviews in Relativity, 12
- Schmoll S., Miller J. M., Volonteri M., Cackett E., Reynolds C. S., Fabian A. C., Brenneman L. W., Miniutti G., Gallo L. C., 2009, The Astrophysical Journal, 703, 2171
- Sikora M., Stawarz Ł., Lasota J.-P., 2007, The Astrophysical Journal, 658, 815
- Sołtan A., 1982, Monthly Notices of the Royal Astronomical Society, 200, 115
- Tanaka T., Shibata M., Sasaki M., Tagoshi H., Nakamura T., 1993, Progress of Theoretical Physics, 90, 65
- Thorne K. S., 1974, The Astrophysical Journal, 191, 507
- Tremaine S., Gebhardt K., Bender R., Bower G., Dressler A., Faber S. M., Filippenko A. V., Green R., Grillmair C., Ho L. C., Kormendy J., Lauer T. R., Magorrian J., Pinkney J., Richstone D., 2002, The Astrophysical Journal, 574, 740
- Trippe S., Paumard T., Ott T., Gillessen S., Eisenhauer F., Martins F., Genzel R., 2007, Monthly Notices of the Royal Astronomical Society, 375, 764
- Turner M., 1977, The Astrophysical Journal, 216, 610
- Vallisneri M., 2008, Physical Review D, 77, 042001
- Volonteri M., 2010, The Astronomy and Astrophysics Review, 18, 279
- Volonteri M., Madau P., Quataert E., Rees M. J., 2005, The Astrophysical Journal, 620, 69
- Volonteri M., Natarajan P., 2009, Monthly Notices of the Royal Astronomical Society, 400, 1911
- Volonteri M., Sikora M., Lasota J.-P., 2007, The Astrophysical Journal, 667, 704
- Wilkins D., 1972, Physical Review D, 5, 814
- Yu Q., Tremaine S., 2002, Monthly Notices of the Royal Astronomical Society, 335, 965
- Yunes N., Sopuerta C. F., Rubbo L. J., Holley-Bockelmann K., 2008, The Astrophysical Journal, 675, 604
- Zoghbi A., Fabian A. C., Uttley P., Miniutti G., Gallo L. C., Reynolds C. S., Miller J. M., Ponti G., 2010, Monthly Notices of the Royal Astronomical Society, 401, 2419

APPENDIX A: WINDOW FUNCTIONS

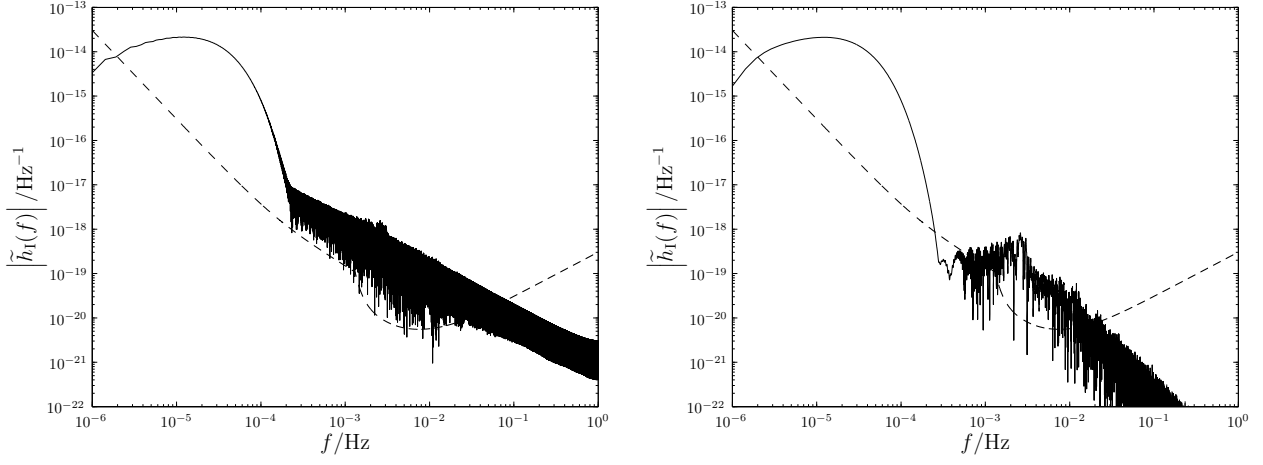
When we perform a Fourier transform using a computer we must necessarily only transform a finite time-span τ . The effect of this is the same as transforming the true, infinite signal multiplied by a unit top-hat function of width equal to the time-span. Fourier transforming this yields the true waveform convolved with a sinc. If $\tilde{h}'(f)$ is the computed Fourier transform then

$$\tilde{h}'(f) = \int_{-\tau/2}^{\tau/2} h(t) e^{2\pi i f t} dt = [\tilde{h}(f) * \tau \text{sinc}(\pi f \tau)], \quad (\text{A1})$$

where $\tilde{h}(f) = \mathcal{F}\{h(t)\}$ is the unwindowed Fourier transform of the infinite signal. This windowing of the data is a problem inherent in the method and results in spectral leakage.

Figure 1(a) shows the computed Fourier transform for an example parabolic encounter. The waveform has two distinct regions: a low-frequency curve, and a high-frequency tail. The low-frequency signal is the spectrum we are interested in; the high-frequency components are the result of spectral leakage. The $\mathcal{O}(1/f)$ behaviour of the sinc gives the shape of the tail. This has possibly been misidentified in figure 8 of Burko & Khanna (2007) as the characteristic strain for parabolic encounters.

Despite being many orders of magnitude below the peak level, the high-frequency tail is still well above the noise



(a) Spectrum using no window. The calculated SNR is $\rho = 12.5$.

(b) Spectrum using a Nuttall window. The calculated SNR is $\rho = 8.5$.

Figure A1. Example spectra calculated using (a) a rectangular window and (b) Nuttall's four-term window with continuous first derivative (Nuttall 1981). The spin of the MBH is $a_* = 0.5$, the mass of the orbiting CO is $\mu = 10M_\odot$, the periapsis is $r_p = 25r_S$ and the inclination is $i = 0.1$. The high-frequency tail is the result of spectral leakage. The level of the LISA noise curve is indicated by the dashed line. The spectra are from detector I, detector II has similar spectra.

curve for a wide range of frequencies. It therefore contributes to the evaluation of any inner products, and could mask interesting features. It is possible to reduce the amount of leakage using apodization: to improve the frequency response of a finite time series one can use a weighting window function $w(t)$ which modifies the impulse response in a prescribed way. The simplest window function is the rectangular (or Dirichlet) window $w_R(t)$; this is just the top-hat described above. Other window functions are generally tapered.⁷ There is a wide range of window functions described in the literature (Harris 1978; Kaiser & Schafer 1980; Nuttall 1981; McKechnan, Robinson & Sathyaprakash 2010). The introduction of a window function influences the spectrum in a manner dependent upon its precise shape; there are two distinct distortions: local smearing due to the finite width of the centre lobe, and distant leakage due to finite amplitude sidelobes. The window function may be optimised such that the peak sidelobe has a small amplitude, or such that the sidelobes decay away rapidly with frequency. Choosing a window function is a trade-off between these various properties, and will depend upon the particular application.

For use with the parabolic spectra, the primary concern is to suppress the sidelobes. Many windows with good sidelobe behaviour exist in the literature; we will consider three: the Blackman-Harris minimum four-term window (Harris 1978; Nuttall 1981)

$$w_{\text{BH}}(t) = \sum_{n=0}^3 a_n^{\text{BH}} \cos\left(\frac{2n\pi t}{\tau}\right), \quad (\text{A2})$$

where

$$\begin{aligned} a_0^{\text{BH}} &= 0.35875, & a_1^{\text{BH}} &= 0.48829, \\ a_2^{\text{BH}} &= 0.14128, & a_3^{\text{BH}} &= 0.01168; \end{aligned} \quad (\text{A3})$$

the Nuttall four-term window with continuous first derivative (Nuttall 1981)

$$w_N(t) = \sum_{n=0}^3 a_n^N \cos\left(\frac{2n\pi t}{\tau}\right), \quad (\text{A4})$$

where

$$\begin{aligned} a_0^N &= 0.355768, & a_1^N &= 0.487396, \\ a_2^N &= 0.144232, & a_3^N &= 0.012604, \end{aligned} \quad (\text{A5})$$

and the Kaiser-Bessel window (Harris 1978; Kaiser & Schafer 1980)

$$w_{\text{KB}}(t; \beta) = \frac{I_0[\beta \sqrt{1 - (2t/\tau)^2}]}{I_0(\beta)}, \quad (\text{A6})$$

where $I_\nu(z)$ is the modified Bessel function of the first kind, and β is an adjustable parameter. Increasing β reduces the peak sidelobe, but also widens the central lobe. The Kaiser-Bessel window has the smallest peak sidelobe, but the worst decay ($1/f$); the Nuttall window has the best asymptotic behaviour ($1/f^3$); the Blackman-Harris window has a peak sidelobe similar to the Nuttall window, and decays asymptotically as fast (slow) as the Kaiser-Bessel window, but has the advantage of having suppressed sidelobes next to the central lobe. Another window has been recently suggested for use with gravitational waveforms: the Planck-taper window (Damour, Iyer & Sathyaprakash 2000; McKechnan et al.

⁷ When using a tapered window function it is important to ensure that the window is centred upon the signal; otherwise the calculated transform will have a reduced amplitude.

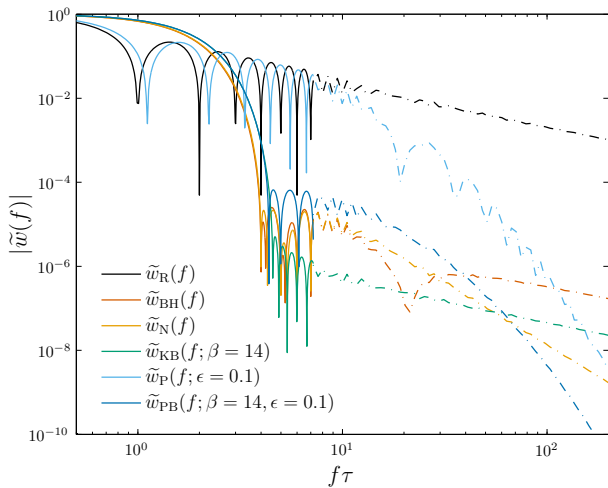


Figure A2. Window function frequency response. To avoid clutter, the response function is only plotted in detail until $f\tau = 8$, above this a smoothed value is used, as indicated by the dot-dashed line. As well as having good asymptotic behaviour, the Planck-taper window has the narrowest main lobe, except for the rectangular window.

2010)

$$w_P(t; \epsilon) = \begin{cases} \frac{1}{\exp(Z_+) + 1} & -\frac{\tau}{2} \leq t < -\tau \left(\frac{1}{2} - \epsilon \right) \\ 1 & -\tau \left(\frac{1}{2} - \epsilon \right) < t < \tau \left(\frac{1}{2} - \epsilon \right) \\ \frac{1}{\exp(Z_-) + 1} & -\tau \left(\frac{1}{2} - \epsilon \right) < t \leq \frac{\tau}{2} \end{cases}, \quad (\text{A7})$$

with

$$Z_{\pm}(t; \epsilon) = 2\epsilon \left[\frac{1}{1 \pm 2(t/\tau)} + \frac{1}{1 - 2\epsilon \pm 2(t/\tau)} \right]. \quad (\text{A8})$$

This was put forward for use with binary coalescences, and has superb asymptotic decay. However, the peak sidelobe is high, which could be disadvantageous for this application. We therefore propose a new window function: the Planck-Bessel window which simply combines the Kaiser-Bessel and Planck-taper windows to produce a window which inherits the best features of both, albeit in a diluted form

$$w_{PB}(t; \beta, \epsilon) = w_P(t; \epsilon)w_{KB}(t; \beta). \quad (\text{A9})$$

The window functions' frequency responses are plotted in Fig. A2. There is no window that performs best everywhere.

Figure A1 shows the computed Fourier transforms for an example parabolic encounter using no window (alternatively a rectangular or Dirichlet window), and the Nuttall four-term window with continuous first derivative.⁸

The waveforms have two distinct regions: a low-frequency curve, and a high-frequency tail. The low-frequency signal is the spectrum we are interested in; the high-frequency components are the result of spectral leakage. Using the Nuttall window, the spectral leakage is

⁸ The Blackman-Harris minimum four-term window, the Kaiser-Bessel window and the Planck-Bessel window give almost identical results.

greatly reduced; the peak sidelobe is lower, and the tail decays away as $1/f^3$ instead of $1/f$.

The choice of window function will influence the results as it changes the form of $\tilde{h}(f)$. The variation in results between windows depends upon the signal: variation is greatest for low frequency bursts, as then there is greatest scope for leakage into the LISA frequency band; variation is least significant for zoom-whirl orbits as then there are strong signals to relatively high frequencies, and spectral leakage is confined to mostly below the noise level. To quantify the influence of window functions, we studied the diagonal elements of the Fisher matrix from a selection of orbits with periapsis ranging from $\sim 5rs$ – $150rs$. For orbits with small periapses all five windows (excluding the rectangular window) produced very similar results: the Planck-taper window differed by a maximum of $\sim 0.5\%$ from the others, which all agreed to better than 0.1% . The worst case results came from the lowest frequency orbits, then the Planck-taper window deviated by a maximum of $\sim 30\%$ in the value for the Fisher matrix elements, the Blackman-Harris deviated by $\sim 20\%$ and the others agreed to better than $\sim 5\%$. The Planck-taper window's performance is limited by its poor sidelobe behaviour; the Blackman-Harris has the worst performance at high frequency.

For this work we have used the Nuttall window. Its performance is comparable to the Kaiser-Bessel and Planck-Bessel windows; however it is computationally less expensive to implement as it does not contain Bessel functions. Results should be accurate to a few percent at worst, and results from closer orbits, which provide better constraints, should be less affected by the choice of window function. Therefore, we are confident that none of our conclusions is sensitive to the particular windowing method implemented.

This paper has been typeset from a TeX/ L^AT_EX file prepared by the author.